

# Temperature-jump solution X-ray scattering reveals distinct motions in a dynamic enzyme

Michael C. Thompson<sup>1</sup>, Benjamin A. Barad<sup>1,2</sup>, Alexander M. Wolff<sup>1,2</sup>, Hyun Sun Cho<sup>3</sup>, Friedrich Schotte<sup>3</sup>, Daniel M. C. Schwarz<sup>1,4</sup> , Philip Anfinrud<sup>3\*</sup> and James S. Fraser<sup>1\*</sup> 

**Correlated motions of proteins are critical to function, but these features are difficult to resolve using traditional structure determination techniques. Time-resolved X-ray methods hold promise for addressing this challenge, but have relied on the exploitation of exotic protein photoactivity, and are therefore not generalizable. Temperature jumps, through thermal excitation of the solvent, have been utilized to study protein dynamics using spectroscopic techniques, but their implementation in X-ray scattering experiments has been limited. Here, we perform temperature-jump small- and wide-angle X-ray scattering measurements on a dynamic enzyme, cyclophilin A, demonstrating that these experiments are able to capture functional intramolecular protein dynamics on the microsecond timescale. We show that cyclophilin A displays rich dynamics following a temperature jump, and use the resulting time-resolved signal to assess the kinetics of conformational changes. Two relaxation processes are resolved: a fast process is related to surface loop motions, and a slower process is related to motions in the core of the protein that are critical for catalytic turnover.**

Protein motions are critical for functions such as enzyme catalysis and allosteric signal transduction<sup>1</sup>, but it remains challenging to study excursions away from the most populated conformations<sup>2</sup>. Traditional methods that utilize X-rays for structural characterization of biological macromolecules, such as crystallography and solution scattering, provide high-quality structural information, but this information is both spatially and temporally averaged because the measurements are performed on large ensembles of molecules and are typically slower than the timescales of molecular motion<sup>2,3</sup>. To some extent, the spatial averaging inherent to X-ray experiments is advantageous, because it reveals the alternative local conformations of a molecule that are significantly populated at equilibrium; however, structural states that are not significantly populated at equilibrium, such as intermediates along a conformational transition pathway, are effectively invisible. The temporal averaging inherent to X-ray experiments also results in a loss of information about how transitions between local alternative conformational states are coupled to one another. To gain kinetic information about molecular motion, researchers often turn to spectroscopic methods, but it can be difficult to correlate spectroscopic observables with high-resolution structural models.

Time-resolved X-ray scattering and diffraction can overcome the limitations of traditional structure determination for studying the dynamics of biomolecules<sup>4–7</sup>. In these experiments, a fast perturbation is applied to the sample to remove it from conformational equilibrium and synchronize conformational changes in a significant fraction of the molecules. Ultrafast X-ray pulses, which are short relative to motions of interest, are then used to perform structural measurements in real time as the system relaxes to a new equilibrium, providing simultaneous structural and kinetic information at high spatial and temporal resolution. Time-resolved X-ray experiments can identify transiently populated structural states along a conformational transition pathway, and reveal kinetic couplings

between conformations<sup>8</sup>. Despite this potential to provide a wealth of information, especially when combined with molecular dynamics simulation<sup>9–12</sup>, time-resolved experiments have not been broadly applied by structural biologists. To date, systems that have been most rigorously studied are those in which a protein conformational change is coupled to excitation of a photoactive chromophore molecule, because the conformational change can be initiated with an ultrafast optical laser pulse (for example, refs. <sup>13–18</sup>). Unfortunately, the number of proteins that undergo specific photochemistry as part of their functional cycle is small, and there is a fundamental need to develop generalized methods that can be used to synchronously excite conformational transitions in any protein molecule and expand the utility of time-resolved structural experiments<sup>19–27</sup>.

Protein structural dynamics are intimately coupled to the thermal fluctuations of the surrounding solvent ('solvent slaving'<sup>28,29</sup>), and thermal excitation of the solvent by infrared laser temperature jump has been used in numerous pump–probe experiments. These experiments work on the principle that absorption of infrared photons excites the O–H stretching modes of water molecules, and the increased vibrational energy is dissipated through increased rotation and translation of the solvent molecules, effectively converting electromagnetic energy into kinetic (thermal) energy. Because this process of solvent heating and subsequent heat transfer to the protein is much faster than the large-scale molecular motions that define protein conformational changes, the sudden temperature jump removes conformational ensembles of protein molecules from their thermal equilibrium so that their structural dynamics can be measured using relaxation methods (Fig. 1a). For example, temperature-jump perturbations have been coupled to ultrafast spectroscopic methods, including Fourier-transform infrared spectroscopy<sup>30,31</sup>, NMR<sup>32–34</sup> and various forms of fluorescence spectroscopy<sup>35,36</sup>, for the study of protein folding and enzyme dynamics. While these methods provide detailed kinetic information, they

<sup>1</sup>Department of Bioengineering and Therapeutic Sciences, University of California, San Francisco, San Francisco, CA, USA. <sup>2</sup>Biophysics Graduate Program, University of California, San Francisco, San Francisco, CA, USA. <sup>3</sup>Laboratory of Chemical Physics, National Institute of Diabetes and Digestive and Kidney Diseases, National Institutes of Health, Bethesda, MD, USA. <sup>4</sup>Chemistry and Chemical Biology Graduate Program, University of California, San Francisco, San Francisco, CA, USA. \*e-mail: [anfinrud@nih.gov](mailto:anfinrud@nih.gov); [jfraser@fraserlab.com](mailto:jfraser@fraserlab.com)

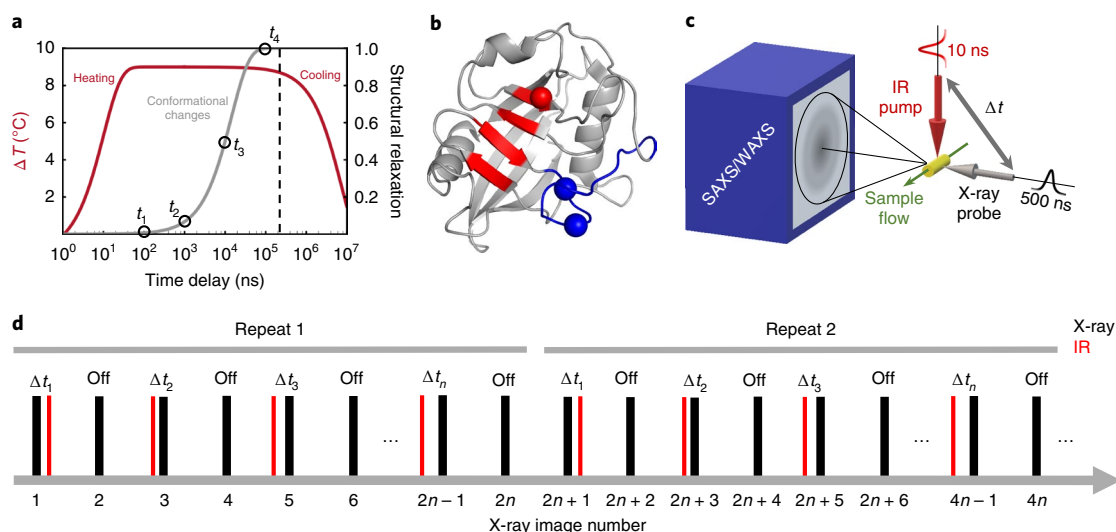


**Fig. 1 | Overview of temperature-jump SAXS/WAXS experiments.** **a**, During a temperature-jump experiment, an infrared (IR) laser pulse, several nanoseconds in duration, vibrationally excites the water O–H stretch and rapidly heats an aqueous solution of protein molecules (red curve). Heating is fast, but kinetic barriers to protein motions cause a lag in the structural relaxation to a new thermal equilibrium of conformational states (grey curve). **b**, Ribbon model depicting a single CypA molecule, with the ‘core’ dynamic residues (linked to catalysis) coloured red and the ‘loop’ region adjacent to the active site (determines substrate specificity) coloured blue. Sites of key mutations (S99T) are identified by spheres at the corresponding C $\alpha$  positions (red: S99T; blue: D66N/R69H). **c**, Schematic of the temperature-jump SAXS/WAXS instrumentation, with key features highlighted. Liquid sample flows through the interaction region, where it interacts with mutually perpendicular IR pump and X-ray probe beams. Both pump and probe sources are pulsed, with a defined time delay between arrivals at the sample. SAXS/WAXS patterns are recorded on a single detector panel. **d**, Data collection sequence used for the temperature-jump experiments. For each pump–probe time delay, a pump–probe measurement (‘laser on’) was performed, followed by a measurement with no application of the pump laser (‘laser off’). On–off pairs with increasing pump–probe time delays were measured in succession until all of the desired delay times were acquired, then the sequence was repeated as many as 50 times to improve the signal-to-noise ratio of the data. Note that the first measurement within each repeat is a control measurement, wherein the probe pulse arrives at the sample before the pump pulse (negative time delay).

yield only very limited structural information about the underlying atomic ensemble. In contrast, the application of temperature jumps to time-resolved X-ray scattering and diffraction has been very limited. Nearly two decades ago, Hori et al.<sup>37</sup> used temperature-jump Laue crystallography to study the initial unfolding step of 3-isopropylmalate dehydrogenase. That study explored only a single pump–probe time delay, which allowed them to observe laser-induced structural changes but precluded kinetic analysis. Within the past two years, the laser temperature-jump method has been paired with X-ray solution scattering to explore the oligomerization of insulin under non-physiological conditions<sup>25,26</sup> and haemoglobin<sup>27</sup>. The results and analysis we present here expand the role of the temperature-jump method in structural biology, by showing that temperature-jump X-ray scattering experiments can be used as a general method to explore the functional, internal dynamics of proteins in solution. Additionally, we provide a detailed outline of a data reduction and analysis procedure suitable for temperature-jump small-angle X-ray scattering (SAXS)/wide-angle X-ray scattering (WAXS) experiments.

The temperature-jump SAXS/WAXS experiments we describe here used human cyclophilin A (CypA)—a proline isomerase enzyme that functions as a protein-folding chaperone and as a modulator of intracellular signalling pathways. CypA has been the subject of many NMR experiments that have identified two primary dynamic features of interest (Fig. 1b). First, the active site-adjacent loops (covering approximately residues 60–80 and hereafter referred to as the ‘loops’ region) are mobile on the millisecond timescale<sup>38</sup>. This region is especially interesting because evolutionarily selected mutations within these loops perturb the dynamics of the loop<sup>39</sup>, alter the binding specificity of CypA for substrates such as immunodeficiency virus capsids<sup>40</sup>, and restrict the host range of these

viruses<sup>41,42</sup>. Second, a group of residues that extends from the active site into the core of the protein (hereafter referred to as the ‘core’ region) has also been shown to be mobile on a millisecond timescale<sup>38</sup>. Subsequent work incorporating multi-temperature X-ray crystallography<sup>43</sup>, mutagenesis<sup>44</sup> and further NMR experiments<sup>45</sup> has established a relationship between catalysis and conformational dynamics of a group of side chains in this region. Motivated by the sensitivity of the conformational state of the active site–core network to temperature<sup>43</sup>, we performed infrared laser-driven temperature jumps on buffered aqueous solutions of CypA and measured subsequent, time-dependent changes in SAXS/WAXS. While our measurements provide only low-resolution structural information, we were able to measure the kinetics of protein conformational changes in CypA. We identified two relaxation processes, and by performing temperature-jump experiments at a range of different temperatures, we were able to calculate thermodynamic properties of the transition states for the underlying conformational transitions. Specific mutants in the ‘loops’ or the ‘core’ regions of CypA show that the two processes are independent, each representing a distinct and uncoupled reaction coordinate on a complex conformational landscape. Collectively, our measurements and analysis show that a wealth of information about a protein’s conformational landscape can be obtained by pairing laser-induced temperature jump with time-resolved X-ray scattering.

## Results

**A method for simultaneous measurement of structural and kinetic details of intrinsic protein dynamics.** To measure protein structural dynamics, we utilized a pump–probe method that pairs an infrared laser-induced temperature jump with global measurement of protein structure via X-ray solution scattering (Fig. 1c).

We performed solvent heating in aqueous protein solutions by exciting the water O–H stretch with mid-IR laser pulses (1,443 nm; 7 ns duration). At regularly defined time delays following the infrared heating pulse (from 562 ns to 1 ms), we probed the sample with high-brilliance synchrotron X-ray pulses from a pink-beam undulator (3% bandwidth at 12 keV; Supplementary Fig. 1) that were approximately 500 ns in duration, and measured X-ray scattering using a large charge-coupled device detector that was capable of capturing small and wide scattering angles on a single panel. Because the duration of the infrared pump pulse was sufficiently short compared with the duration of the X-ray probe, the heating was effectively instantaneous with respect to the relaxation processes we were able to observe. Data were collected as interleaved ‘laser on’ and ‘laser off’ X-ray scattering images, so that each pump–probe measurement could be paired to a measurement made immediately before application of the pump laser (Fig. 1d). We measured 27 unique pump–probe time delays across four decades of time spanning from 562 ns to 1 ms, performing 50 repeat measurements for each time delay. For each detector image, the individual pixel values were azimuthally averaged as a function of the scattering vector magnitude,  $q$ , to give one-dimensional scattering intensity profiles ( $I(q)$  curves). All scattering profiles were scaled to a single reference, and the data were analysed as described below. These pump–probe measurements allowed us to monitor structural changes within the ensemble of heated molecules in real time as the system relaxed to a new thermal equilibrium following temperature jump (Fig. 1a). Additional details about the instrumentation used for our experiments are available in the Supplementary Methods.

**Calibrating the magnitude of the temperature jump.** Because the isothermal compressibility of liquid water is highly temperature dependent<sup>46</sup>, X-ray scattering from the bulk solvent acts as an exquisitely sensitive thermometer that can be used to calibrate the magnitude of the temperature jump in our experiments<sup>9,25,27,47,48</sup>. Our instrument configuration allowed us to record low-angle protein scattering (SAXS) and high-angle solvent scattering (WAXS) on the same detector image, enabling simultaneous measurement of CypA structure and water temperature. A method based on singular value decomposition of a matrix constructed from the scattering curves provided a simple way to measure the magnitude of the laser-induced temperature jump (Supplementary Data). The singular value decomposition (SVD) analysis showed that the average temperature jump produced by our infrared heating pulse was approximately 10.7°C, and allowed us to judge when cooling of the system became significant, so that we could identify the maximum pump–probe time delay that was valid for our relaxation analysis. Additionally, the SVD analysis revealed that following laser temperature jump, the solvent reaches a new thermal equilibrium faster than the measurement dead time of our experiment (562 ns). This observation is consistent with other work, in which changes to the structure of bulk solvent following laser temperature jump have been shown to equilibrate within roughly 200 ns<sup>49</sup>.

**Temperature jump produces changes in the X-ray scattering profile of CypA.** To determine the effect of the temperature jump, we initially averaged all data for a given time delay (Supplementary Fig. 2), examined the scattering profiles for differences, and observed a small laser-induced change in the low- $q$  region of the scattering profiles. Next, we exploited the interleaved data collection scheme (Fig. 1d) to increase the sensitivity of the experiment. We calculated the ‘on–off difference’ between the paired ‘laser on’ and ‘laser off’ scattering profiles. Following subtraction, we binned the ‘on–off difference’ scattering curves according to the associated pump–probe time delay, performed an iterative chi-squared test to remove outliers, and averaged the calculated differences for all repeat measurements (Supplementary Methods). This subtraction and averaging

removed systematic errors that accumulated over long experiments, resulting in accurate measurements of difference signals as a function of the pump–probe time delay. Scattering differences at high  $q$  (1.0–4.2 Å<sup>-1</sup>) were used to calibrate the final sample temperature after laser illumination (Supplementary Data), while differences at low  $q$  (0.03–0.3 Å<sup>-1</sup>) were analysed in the context of the average physical dimensions and scattering density of the CypA ‘protein particle’. Here, we use the phrase ‘protein particle’ to describe the protein molecule plus the ordered solvent bound to its surface, since both the protein and its hydration layer have electron densities that differ from bulk solvent, and therefore contribute to the observed X-ray scattering by the CypA solution. Identical temperature-jump measurements were performed on protein samples and on samples consisting of buffer only without protein, and an additional step of scaling and subtraction isolated the signal changes at low  $q$  due only to the protein (Supplementary Fig. 2).

**Time-resolved changes in small-angle X-ray scattering.** Comparison of difference scattering curves calculated for 27 unique time delays revealed a time-dependent change in X-ray scattering by the protein, demonstrating that the modest temperature jump we introduced was capable of exciting protein dynamics that could be observed in real time. The difference curves calculated from our data, showing the contribution of the protein to time-resolved changes in the SAXS/WAXS signal, have features in the low- $q$  ( $q=0.03$ – $0.3$  Å<sup>-1</sup>) region (Fig. 2a). The time-resolved differences are approximately the same in magnitude and direction as differences between static temperature measurements performed on samples equilibrated to temperatures that differ by 10°C, and correspond to the ‘laser on’ and ‘laser off’ temperatures (Supplementary Fig. 3). Qualitatively, the time-resolved on–off differences show that the overall low-angle scattering and extrapolated value of  $I(0)$  are reduced within the measurement dead time of our experiment (562 ns), then begin to increase slightly over the next few microseconds before decreasing further at longer pump–probe time delays out to 562 μs. The observed ‘laser on–off’ difference in  $I(0)$  is approximately 3% of the total observed signal, with one-third of that signal change occurring in the time regime that can be resolved by our measurements. Additional static measurements as a function of both CypA concentration and temperature allowed us to characterize and correct for the effect of interparticle interactions, and to determine that their contribution to the X-ray scattering is temperature independent over the relevant temperature range (Supplementary Data).

Changes in low-angle scattering generally reflect changes in the overall size and shape of the particles in solution, and changes in  $I(0)$  result from changes to the scattering density of the particle (that is, the number of excess electrons in the particle relative to the bulk solvent that it displaces). The observed reduction of both quantities indicated shrinkage of the scattering particles, and a decrease in their scattering density. The on–off difference for our shortest pump–probe time delay (562 ns) is significantly different from 0 at low scattering angles (a reduction in  $I(0)$  of approximately 2%), showing the existence of structural changes that are faster than the measurement dead time of our experiments. We hypothesize that the physical basis for this fast signal change is a combination of thermal disorder and thermal expansion effects (Supplementary Data), possibly including a temperature-induced loss (or ‘melting’) of ordered solvent within the protein hydration shell. Previous work, such as measurement of ‘protein-quake’ motions in photoactive systems<sup>9,50</sup>, has shown that vibrational energy transfer is fast in proteins, and we expect that the onset of thermal disorder following temperature jump happens on a similar timescale, within hundreds of picoseconds. Furthermore, thermal expansion of solvent following temperature jump is well known to equilibrate within approximately 200 ns<sup>25,47,48</sup>, and it is reasonable to assume that protein thermal expansion may occur on a

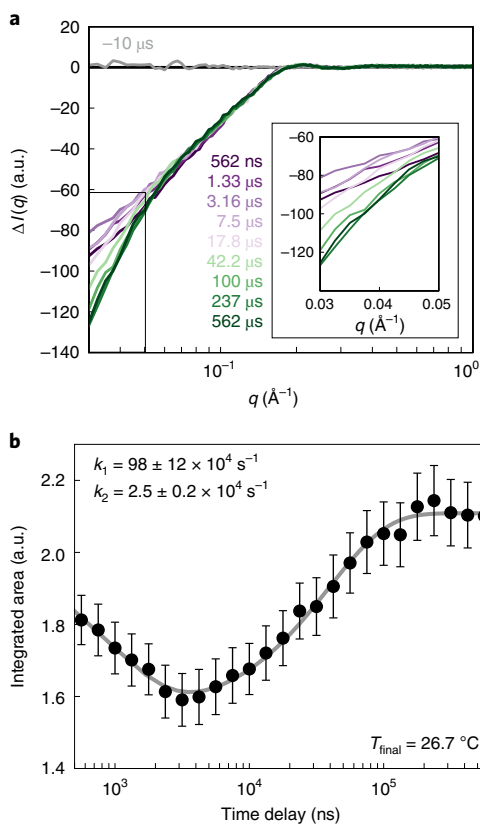


**Fig. 2 | Temperature-jump data allow kinetic modelling of conformational dynamics.** **a**, A series of averaged time-resolved difference X-ray scattering curves is shown for a subset of our temperature-jump data (10 out of 26 unique time delays). Data at low  $q$  are plotted on a linear  $q$  scale in the inset. **b**, The area under the averaged difference scattering curve in the  $q = 0.03\text{--}0.05 \text{ \AA}^{-1}$  region was integrated for all measured pump-probe time delays, and the resulting absolute values and their standard deviations (error bars) are plotted as a function of the pump-probe time delay. The plotted data suggest the existence of multiple relaxation processes, but not time dependent over the pump-probe time delays we explored, confirming that the process is faster than the measurement dead time of our experiment. The physical details and kinetics of these fast processes, although interesting, are invisible to our experiment, and it is impossible to disentangle and quantify the exact contribution of each phenomenon to the fast signal decrease that we observe. Therefore, our analysis focused on structural dynamics that occur in the microsecond regime, which is resolved by our measurements. In contrast, ultrafast single pulses from synchrotrons (pulse duration:  $\sim 100$  ps) or X-ray free-electron lasers (pulse duration:  $\sim 10$  fs) offer the opportunity to study fast timescale processes using temperature jump; however, a major consideration for temperature-jump SAXS/WAXS experiments on faster timescales is the additional complexity in signal interpretation resulting from the complex dynamics of the solvent that immediately follow laser heating<sup>25,47,48</sup> but equilibrate within the dead time of the experiments reported here.

similar timescale. The notion that thermal disorder and expansion occur rapidly in our system is experimentally supported by Kratky plots created from our static and temperature-jump data, which suggest a slight increase in protein flexibility without unfolding (Supplementary Fig. 4). The effect is temperature dependent, but not time dependent over the pump-probe time delays we explored, confirming that the process is faster than the measurement dead time of our experiment. The physical details and kinetics of these fast processes, although interesting, are invisible to our experiment, and it is impossible to disentangle and quantify the exact contribution of each phenomenon to the fast signal decrease that we observe. Therefore, our analysis focused on structural dynamics that occur in the microsecond regime, which is resolved by our measurements. In contrast, ultrafast single pulses from synchrotrons (pulse duration:  $\sim 100$  ps) or X-ray free-electron lasers (pulse duration:  $\sim 10$  fs) offer the opportunity to study fast timescale processes using temperature jump; however, a major consideration for temperature-jump SAXS/WAXS experiments on faster timescales is the additional complexity in signal interpretation resulting from the complex dynamics of the solvent that immediately follow laser heating<sup>25,47,48</sup> but equilibrate within the dead time of the experiments reported here.

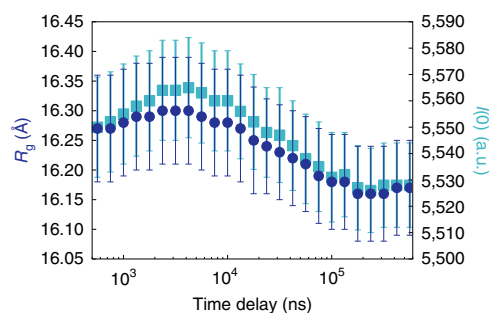


**Fig. 3 | Time-resolved Guinier analysis.** Changes in the average physical parameters of CypA protein particles in the ensemble were estimated by performing Guinier analysis on the time-resolved scattering data. Consistent with our kinetic analysis, the radius of gyration ( $R_g$ ) of the average CypA particle in solution first increases and then decreases as a function of time following the temperature jump. Additionally, the value of  $I(0)$  extrapolated from the Guinier analysis shows an analogous increase and decrease, suggesting that the change in the particle size is coupled to a change in its average electron density, which is probably due to the acquisition and loss of water molecules from the solvation shell as the protein swells and then shrinks. Error bars represent standard deviations of the calculated quantities based on propagation of measurement standard deviations.

**Kinetic modelling of structural dynamics from time-resolved scattering differences.** Our time-resolved measurements of scattering differences allowed us to model the kinetics of global structural changes induced by the temperature jump (Supplementary Methods). We integrated the area under each of our time-resolved difference curves in the  $q = 0.03\text{--}0.05 \text{ \AA}^{-1}$  region and plotted the absolute value of the area as a function of the associated pump-probe time delay (Fig. 2b). Based on the apparent shape of the area versus time delay plot, we reasoned that a two-step kinetic model would be needed to fit the data, since the area first decreases and then increases as a function of time delay. We fit the observed data to a two-step model of relaxation kinetics (independent steps) using a nonlinear least-squares curve-fitting algorithm, and calculated rates of  $98 \times 10^4 \pm 12 \times 10^4 \text{ s}^{-1}$  for the fast process ( $k_1$ ) and  $2.5 \times 10^4 \pm 0.2 \times 10^4 \text{ s}^{-1}$  for the slow process ( $k_2$ ) at  $26.7 \text{ }^\circ\text{C}$  ( $299.7 \text{ K}$ ). The errors calculated for these rates were determined using a bootstrap analysis<sup>51</sup>. We note that while other experimenters have employed SVD for kinetic analysis of time-resolved scattering, in our case, implementation of this method produced comparable results to the integration analysis, as one singular vector dominated the time-dependent signal identified by the SVD (Supplementary Fig. 5).

In addition to performing kinetic analysis, we also utilized the on-off difference curves to generate  $I(q)$  scattering curves, which represent the time-dependent X-ray scattering from the CypA sample, but are generated in a manner that makes use of the paired ‘laser on’ and ‘laser off’ measurements to reduce the effects of systematic error (Supplementary Methods). We subsequently used these scattering curves for Guinier analysis (Supplementary Methods) to determine how the radius of gyration ( $R_g$ ) of the average CypA particle in the conformational ensemble changes as a function of time following the temperature jump (Fig. 3). This analysis showed that after the temperature jump, the average CypA particle shrinks in the dead time of our experiment; however, within a few microseconds of the temperature jump, a fast structural transition (described by  $k_1$  in our kinetic analysis) causes the average CypA particle to expand subtly. While the increase in the calculated radius of gyration is small relative to the error on the Guinier fit for any single data point, our conclusion that the particle is expanding is supported by multiple time

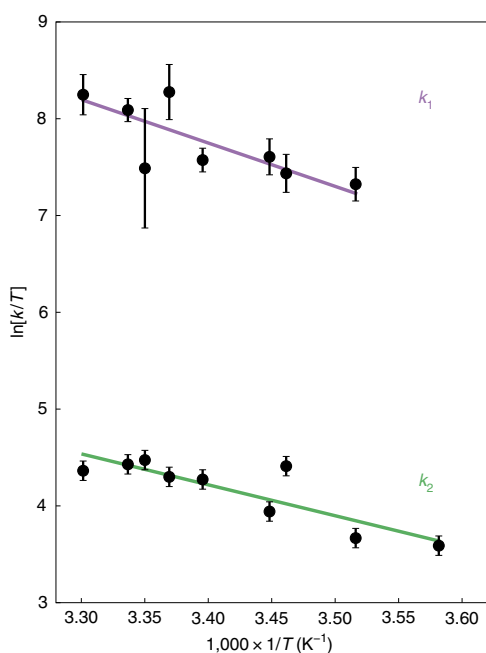


**Fig. 4 | Eyring analysis of transition-state thermodynamics.** Linear Eyring plots are shown for each of the two relaxation processes observed in our temperature-jump experiments with CypA. Both processes show Arrhenius behaviour over the temperature range we explored, and the apparent linear relationship between  $1/T$  and  $\ln[k/T]$  justifies the use of the linear Eyring equation (equation (1)) to fit the data and characterize the thermodynamics of the transition states. Data points represent rates determined from the kinetic analysis, and error bars represent the standard deviations of the rates based on propagation of the measurement standard deviations and bootstrap analysis (see Supplementary Methods). The fit to the linear Eyring equation for the fast process ( $k_1$ ) is shown in purple, and the fit for the slow process ( $k_2$ ) is shown in green.

points and kinetic analysis of the integrated area under difference scattering curves. Following this fast increase in  $R_g$ , a second, slower process (described by  $k_2$  in our kinetic analysis) reverses this trend, causing the average CypA particle to shrink again.

To learn more about the conformational transitions in CypA that are excited by the temperature jump, we repeated the experiment at multiple different jumped (final) temperatures ranging from 6.2–29.9 °C (279.2–302.9 K). We modelled the kinetics of the SAXS/WAXS signal changes to observe how the relaxation rates changed as a function of temperature. The calculated rates ( $k_1$  and  $k_2$ ) for all temperatures are provided in Supplementary Table 1. We analysed the temperature dependence of these rates, which provided insight into the thermodynamics of the transition states for the two processes. We plotted  $\ln[k/T]$  versus  $1/T$  (Fig. 4), and noted that for both processes the relationships appeared to be linear. Therefore, we calculated enthalpies and entropies of activation for each of the two processes by fitting the data to the linearized Eyring equation:

$$\ln\left[\frac{k}{T}\right] = \left(\frac{\Delta H^\ddagger}{R} \times \frac{1}{T}\right) + \frac{\Delta S^\ddagger}{R} + \ln\left[\frac{k_B}{h}\right] \quad (1)$$

where  $R$  is the gas constant,  $k_B$  is the Boltzmann constant and  $h$  is Planck's constant. The enthalpies of activation ( $\Delta H^\ddagger$ ) and entropies of activation ( $\Delta S^\ddagger$ ) and their standard deviations are given in Table 1. The fast process ( $k_1$ ) has a large, positive enthalpy of activation, but this is partially offset by a slightly positive entropy of activation. Formation of the transition state during the slow process ( $k_2$ ) has a smaller enthalpic cost, but is also entropically disfavoured. We note

**Table 1 | Thermodynamic properties of transition states**

	$\Delta H^\ddagger$ ( $10^3$ J mol <sup>-1</sup> )	$\Delta S^\ddagger$ (J mol <sup>-1</sup> K <sup>-1</sup> )
Fast process ( $k_1$ )	37 ± 8	32 ± 26
Slow process ( $k_2$ )	27 ± 3	-34 ± 11

Enthalpies ( $\Delta H^\ddagger$ ) and entropies ( $\Delta S^\ddagger$ ) of activation, and their standard deviations based on propagation of measurement standard deviations through all analysis steps, for the fast ( $k_1$ ) and slow ( $k_2$ ) processes observed for wild-type CypA, calculated from Eyring analysis.

that the lowest temperature measurement (279.2 K) was not used in the Eyring analysis of the fast process ( $k_1$ ) because the error on the measured rate was large due to the low magnitude of the overall time-resolved signal changes at this temperature.

**CypA mutations with distinct effects on conformational dynamics alter time-resolved signal changes.** The time-resolved signal changes that we attributed to wild-type CypA were observed only at low scattering angles; therefore, the resulting structural information had very limited resolution. To gain a better understanding of the structural transitions excited by the temperature jump, we next studied two specific CypA mutants, S99T (in the 'core' region; red in Fig. 1b) and NH (D66N/R69H in the 'loops'; blue in Fig. 1b). The conformational dynamics of these two variants of the enzyme each differ from the wild type in distinct ways: S99T is catalytically impaired due to a loss of rotameric exchange in a key network of residues, whereas NH alters the substrate specificity of CypA by enhancing the dynamics of the surface-exposed loops adjacent to the active site. Importantly, NMR relaxation measurements indicate that S99T perturbs the active site but not the loops<sup>44</sup>, and that NH only perturbs the loops<sup>39</sup>.

We observed that both S99T and NH mutants showed time-resolved SAXS signal changes that differed from the wild-type enzyme. Both mutants showed a fast signal change that occurred within the measurement dead time of the experiment, similar to what was observed for the wild-type enzyme, and consistent with these changes being largely due to thermal expansion or temperature-dependent changes to the solvation shell. Beyond the initial fast loss of scattering intensity that was observed (and nearly identical) for all three CypA variants we studied (wild type, S99T and NH), the evolution of the time-resolved signals for each of the two mutants differed substantially from the wild type and from one another. In the S99T mutant (Fig. 5a), we observed only the fast decrease ( $k_1$ ) of the integrated area under the difference curve ( $q=0.03$ – $0.05$  Å<sup>-1</sup>), and a striking absence of the subsequent increase ( $k_2$ ) in the integrated area at longer time delays that was observed for the wild-type enzyme. In contrast, for NH, the plot of integrated area under the difference curve as a function of the time delay (Fig. 5b) appears to lack the initial fast decrease ( $k_1$ ), but it does appear to retain the slower signal change ( $k_2$ ) that results in an increase for this quantity at longer time delays. We found that for the mutants, the two-step kinetic model that was fit to the wild-type data yielded at least one rate with a large error. For the S99T mutant, the first step ( $k_1$ ) was well fit but the second step ( $k_2$ ) was poorly fit, while the opposite was true for the NH variant. After visual inspection, we chose to use a single-step kinetic model to fit the data for the S99T and NH mutants, and the calculated rates for the two mutants ( $k_1$  for S99T and  $k_2$  for NH) are also given in Supplementary Table 1. Plots of the residuals for these fits revealed no structure, suggesting that a single-step kinetic model is sufficient to explain the data for the CypA mutants. In contrast, fitting kinetic data collected for the wild-type enzyme using a single-step model results in residuals with exponential character, and a two-step kinetic model is needed to reduce the error in the fit (Supplementary Fig. 6).

Our measurements of the S99T and NH variants of CypA clearly show that mutations that are known to impinge on the activity and

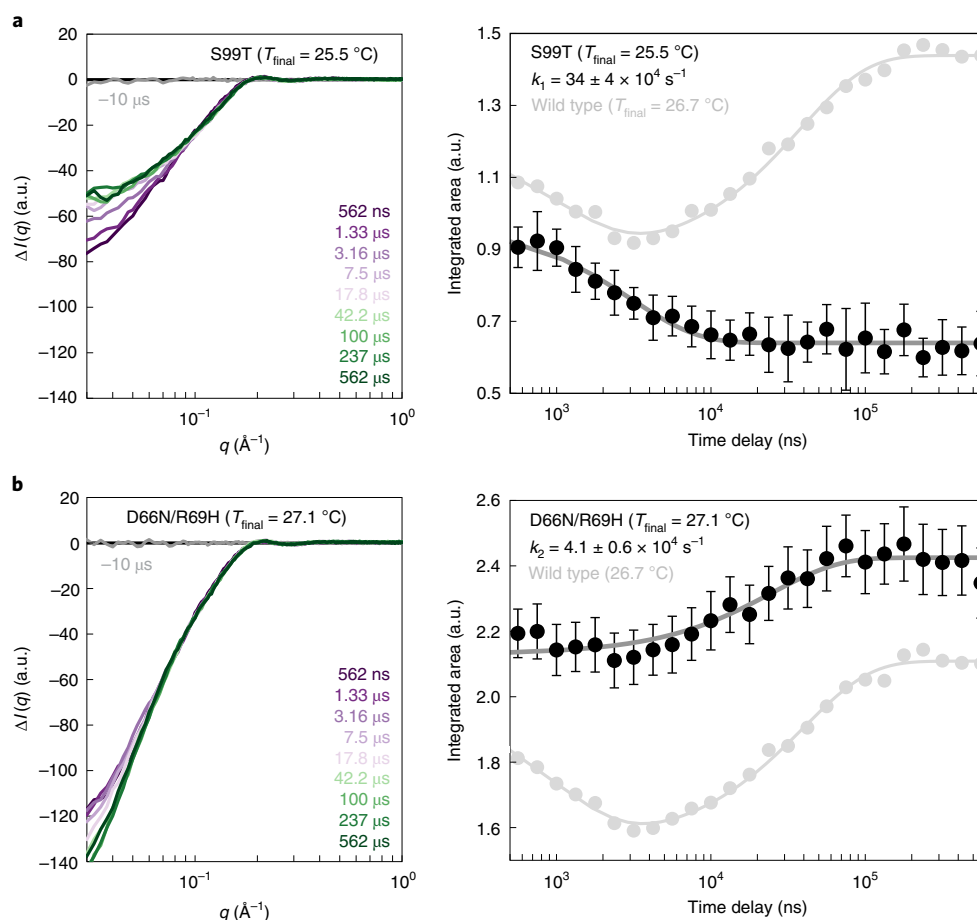


**Fig. 5 | Kinetic analysis of CypA variants.** **a,b**, Two CypA mutants (S99T (**a**) and D66N/R69H (**b**)), with distinct effects on the enzyme's function, show the link between the observed temperature-jump signal and functional dynamics. The data are presented in the same manner as for the wild-type enzyme shown in Fig. 4. Left panels show a subset of averaged difference scattering curves for several pump-probe time delays. Data points in the right panels represent the absolute value of the integrated area under the corresponding averaged difference scattering curve in the  $q=0.03\text{--}0.05\text{ \AA}^{-1}$  region, and the error bars represent standard deviations. In **a**, the S99T mutant, which displays defective catalytic function, shows only the fast relaxation process ( $k_1$ ) and lacks the slower process ( $k_2$ ). In **b**, the D66N/R69H (NH) mutant, with altered substrate specificity, shows the slow relaxation process ( $k_2$ ) and lacks the faster process ( $k_1$ ).

specificity of the enzyme also perturb the observed time-resolved signal relative to the wild type in our temperature-jump experiments. Most notably, the slow relaxation process (modelled by  $k_2$ ) is shared only by the catalytically competent wild-type and NH variants, and its absence from the S99T variant suggests that the underlying conformational change is related to the catalytically coupled motions that are arrested by the S99T mutation. These results indicate that temperature-jump experiments are capable of exciting and measuring functionally relevant, intramolecular structural dynamics of proteins, even when the data are limited to relatively low scattering angles.

## Discussion

Time-resolved temperature-jump X-ray scattering experiments have the potential to be a powerful tool for understanding the complex dynamics of protein molecules, such as the model enzyme CypA, which has no intrinsic photoactivity. In our experiments, temperature jumps of 10–11 °C modified the CypA conformational ensemble, producing a clear, time-dependent change at low scattering angles. Because the time-resolved scattering changes could be observed only at low  $q$ , we demonstrated that interparticle spacings (quantified by the structure factor,  $S(q)$ ) were temperature independent, and that

the changes were due to structural rearrangements within the protein particle. Guinier analysis of time-resolved scattering curves allowed us to track changes in the average radius of gyration ( $R_g$ ) of the protein particles, which include the CypA molecules plus their ordered solvation shells. This signal change comprises an initial reduction in low-angle scattering that occurs within the measurement dead time of our experiment, followed by a small increase in low-angle scattering that equilibrates within a few microseconds ( $k_1=98\pm 12\times 10^4\text{ s}^{-1}$  at 26.7 °C), and finally a further reduction in low-angle scattering that equilibrates within tens of microseconds ( $k_2=2.5\pm 0.2\times 10^4\text{ s}^{-1}$  at 26.7 °C). High-angle scattering differences required for atomistic structural interpretation were not observed due to signal-to-noise considerations. We suspect that high-angle features in time-resolved difference scattering curves may be especially weak for proteins such as CypA, in which conformational motions involve correlated shifts of atoms that can preserve many properties of short-range structure.

This analysis suggests a model in which the scattering density of the CypA particle (protein and ordered solvent) first increases and then decreases after excitation by the temperature jump. By performing temperature-jump experiments over a range of temperatures, we discovered that both the fast and slow processes we observed could be described using Arrhenius kinetics. An Eyring analysis revealed

relatively large, positive enthalpies of activation for both processes, consistent with the idea that conformational changes generally require breakage of existing interactions in both the protein and the solvent. The activation enthalpy for the fast process ( $k_1$ ) is larger, but the overall activation energy is lower because of a favourable activation entropy. The opposite is true for the slower process ( $k_2$ ), which has a smaller overall activation enthalpy, but a disfavoured activation entropy. We used the S99T and NH variants of CypA to disentangle the nature of these processes and their associated functions. The S99T mutant is capable of undergoing the fast ( $k_1$ ) expansion process, but does not experience the subsequent slow ( $k_2$ ) shrinkage. NMR and crystallography have shown that this mutation arrests the conformational exchange of the 'core' catalytic network of residues in CypA by creating steric hindrance, strongly favouring a minor conformation of the wild-type enzyme<sup>45</sup>. This interpretation suggests that the internal rearrangements are related to the  $k_2$  process. However, there is a separation of timescales between the NMR results, which indicate millisecond dynamics in the 'core' region, and the temperature-jump SAXS results here, which indicate microsecond dynamics. This discrepancy may reflect coupled processes that are related by a population-shuffling mechanism<sup>52</sup> and agree with a broad timescale range of side chain dynamics in CypA uncovered by molecular dynamics experiments<sup>53</sup>. In contrast with the S99T mutant, the NH variant lacks the initial fast signal change ( $k_1$ ) in our temperature-jump experiments, but clearly retains the slow ( $k_2$ ) signal. NMR and crystallographic studies of the D66N/R69H (NH) double mutant showed that it maintains wild-type catalytic motions, but breakage of several hydrogen-bonding interactions results in enhanced flexibility of a surface loop adjacent to the active site and altered substrate specificity<sup>39</sup>. NMR experiments with NH have shown that the loop motions still occur, but at an increased rate that renders them invisible to our experiments. Therefore, we hypothesize that the loop motions are responsible for the fast ( $k_1$ ) signal in wild-type CypA and S99T, where these motions have been shown (by NMR) to be unperturbed<sup>44</sup>.

The assignment of the motions responsible for the experimentally observed  $R_g$  and  $I(0)$  changes by mutational analysis is also consistent with X-ray crystal structures of CypA. Using a room temperature X-ray crystal structure of wild-type CypA (Protein Data Bank ID: 3K0N), we calculated the  $R_g$  of the enzyme with the core catalytic network (Arg55, Met61, Ser99 and Phe113) in both the major and minor conformational states, and found that the predicted  $R_g$  of the minor state is 0.07 Å smaller than the major state (14.09 versus 14.16 Å, for protein atoms only). In addition to decreasing the  $R_g$  of the protein, conversion from the major to the minor state also results in a small reduction in solvent-exposed surface area, which would necessarily reduce the size of the protein solvation layer. While the reduction of the protein's  $R_g$  makes it more compact, and therefore should increase  $I(0)$  because the protein has become more dense, the loss of material from the solvation layer opposes this effect, probably leading to the observed decrease in the scattering density of the CypA particle and reduction in  $I(0)$ . This coupling of  $R_g$  changes with changes in the solvent-exposed surface area of the protein can potentially explain the observed correlation between  $R_g$  and  $I(0)$  changes calculated from our time-resolved scattering data. Additionally, the increase in the average  $R_g$  and  $I(0)$  during the faster process ( $k_1$ ) is consistent with the loops sampling an expanded conformational ensemble (with increased surface area), as indicated by recent exact nuclear Overhauser effect NMR ensembles<sup>34</sup>. Our kinetic modelling of the wild-type and mutant data suggests that two dynamic modes are observed, each of which is individually perturbed by different mutations. However, the extent to which the observed motions are coupled is unclear from our measurements. The S99T variant clearly shows that the fast motion can occur independent of the slower motion, because S99T is known to have arrested slow dynamics. In contrast, the fast motion we observe is

likely to be accelerated by the NH mutation, becoming too fast for us to observe rather than being impeded. Therefore, we are unable to determine whether the fast motion is a requisite first step that precedes the slower motion.

Time-resolved X-ray structural measurements are critical for decoupling the experimental signatures of conformational changes that can become convoluted by the spatial and temporal averaging that is inherent to traditional X-ray experiments. If one were to assess traditional, static SAXS data for CypA, they would find that increasing the temperature of the sample results in a decrease in the average particle size at equilibrium. These static measurements as a function of equilibrium temperature fail to capture that the temperature change actually perturbs two distinct protein motions, which have the opposite effect on the enzyme's global structural characteristics. This information can only be obtained through a time-resolved experiment, which is able to separate the effects of these two motions because they have substantially different rates. The ability to dissect individual conformational motions and measure their rates is important for understanding processes involving complex protein dynamics. Many of these dynamic processes, including allostery<sup>55–58</sup> and enzyme catalysis<sup>59–63</sup>, involve extensive reorganization of interactions between the protein and its ordered solvation shell, which are key contributors to the energetics that govern protein motions<sup>28,29,64–68</sup>. Because X-ray solution scattering experiments report on the structure of a protein and the ordered solvent molecules that constitute its solvation shell<sup>69–72</sup>, the widespread application of time-resolved SAXS/WAXS experiments will enhance our understanding of protein motions, including how they are driven by solvent dynamics, especially when they can be combined with longer and increasingly detailed molecular dynamics simulations to provide atomic-scale insight into the underlying structural changes<sup>9–12</sup>.

For time-resolved experiments to enter the mainstream of structural biology, it is necessary to create general perturbations that can be applied universally (to any protein of interest), and our results establish that temperature jump can excite functional intramolecular protein motions for time-resolved X-ray structural measurements. The intrinsic motions of proteins and other biological macromolecules are naturally driven by thermal fluctuations, which makes temperature jump an ideal perturbation for studying their dynamics using time-resolved X-ray scattering. Consistent with this idea, a growing number of X-ray diffraction studies across multiple systems have shown that conformational equilibria, which are sensitive to temperature perturbation, are the same ones exploited by evolution to create new functions<sup>73,74</sup>, by medicinal chemists in identifying novel small-molecule binding sites<sup>75–77</sup>, and by enzymes during their catalytic cycles<sup>44,78,79</sup>, paving the way for time-resolved measurements on a broad variety of biochemical systems. Temperature-jump solution scattering experiments are powerful tools for understanding protein dynamics, especially when they can be paired with atomistic simulations<sup>69</sup>, or with crystal structures of alternative conformations and functional perturbations, as demonstrated here. In the future, functional perturbations such as the mutations that we used to study CypA, or binding of chemical ligands, could be paired with time-resolved structural data from temperature-jump experiments to provide insight into how disease alleles or drug molecules impinge on protein dynamics.

#### Data availability

Scattering data are deposited at NIH Figshare (<https://doi.org/10.35092/yhjc.9177143>). Additional information and files are available from the corresponding author upon reasonable request.

#### Code availability

All Python scripts used for analysis of integrated X-ray scattering curves are publicly available from GitHub (<https://github.com/>

fraser-lab/solution\_scattering). A code release checkpoint containing the exact scripts used in this work is available via Zenodo (<https://doi.org/10.5281/zenodo.3355707>).

Received: 3 December 2018; Accepted: 9 August 2019;

Published online: 16 September 2019

## References

- Henzler-Wildman, K. & Kern, D. Dynamic personalities of proteins. *Nature* **450**, 964–972 (2007).
- Van den Bedem, H. & Fraser, J. S. Integrative, dynamic structural biology at atomic resolution—it's about time. *Nat. Methods* **12**, 307–318 (2015).
- Bottaro, S. & Lindorff-Larsen, K. Biophysical experiments and biomolecular simulations: a perfect match? *Science* **361**, 355–360 (2018).
- Schmidt, M. Time-resolved macromolecular crystallography at modern X-ray sources. *Methods Mol. Biol.* **1607**, 273–294 (2017).
- Neutze, R. & Moffat, K. Time-resolved structural studies at synchrotrons and X-ray free electron lasers: opportunities and challenges. *Curr. Opin. Struct. Biol.* **22**, 651–659 (2012).
- Schotte, F. et al. Watching a signaling protein function in real time via 100-ps time-resolved Laue crystallography. *Proc. Natl Acad. Sci. USA* **109**, 19256–19261 (2012).
- Cho, H. S. et al. Picosecond photobiology: watching a signaling protein function in real time via time-resolved small- and wide-angle X-ray scattering. *J. Am. Chem. Soc.* **138**, 8815–8823 (2016).
- Schlichting, I. & Miao, J. Emerging opportunities in structural biology with X-ray free-electron lasers. *Curr. Opin. Struct. Biol.* **22**, 613–626 (2012).
- Arnlund, D. et al. Visualizing a protein quake with time-resolved X-ray scattering at a free-electron laser. *Nat. Methods* **11**, 923–926 (2014).
- Berntsson, O. et al. Sequential conformational transitions and  $\alpha$ -helical supercoiling regulate a sensor histidine kinase. *Nat. Commun.* **8**, 284 (2017).
- Takala, H. et al. Signal amplification and transduction in phytochrome photosensors. *Nature* **509**, 245–248 (2014).
- Brinkmann, L. U. L. & Hub, J. S. Ultrafast anisotropic protein quake propagation after CO photodissociation in myoglobin. *Proc. Natl Acad. Sci. USA* **113**, 10565–10570 (2016).
- Barends, T. R. M. et al. Direct observation of ultrafast collective motions in CO myoglobin upon ligand dissociation. *Science* **350**, 445–450 (2015).
- Coquelle, N. et al. Chromophore twisting in the excited state of a photoswitchable fluorescent protein captured by time-resolved serial femtosecond crystallography. *Nat. Chem.* **10**, 31–37 (2018).
- Pande, K. et al. Femtosecond structural dynamics drives the *trans/cis* isomerization in photoactive yellow protein. *Science* **352**, 725–729 (2016).
- Kern, J. et al. Structures of the intermediates of Kok's photosynthetic water oxidation clock. *Nature* **563**, 421–425 (2018).
- Nogly, P. et al. Retinal isomerization in bacteriorhodopsin captured by a femtosecond X-ray laser. *Science* **361**, eaat0094 (2018).
- Malmerberg, E. et al. Time-resolved WAXS reveals accelerated conformational changes in iodoretinal-substituted proteorhodopsin. *Biophys. J.* **101**, 1345–1353 (2011).
- Hekstra, D. R. et al. Electric-field-stimulated protein mechanics. *Nature* **540**, 400–405 (2016).
- Schlichting, I. et al. Time-resolved X-ray crystallographic study of the conformational change in Ha-Ras p21 protein on GTP hydrolysis. *Nature* **345**, 309–315 (1990).
- Stoddard, B. L., Cohen, B. E., Brubaker, M., Mesecar, A. D. & Koshland, D. E. Jr Millisecond Laue structures of an enzyme-product complex using photocaged substrate analogs. *Nat. Struct. Biol.* **5**, 891–897 (1998).
- Josts, I. et al. Photocage-initiated time-resolved solution X-ray scattering investigation of protein dimerization. *IUCr* **5**, 667–672 (2018).
- Rimmerman, D. et al. Revealing fast structural dynamics in pH-responsive peptides with time-resolved X-ray scattering. *J. Phys. Chem. B* **123**, 2016–2021 (2019).
- Olmos, J. L. Jr et al. Enzyme intermediates captured 'on the fly' by mix-and-inject serial crystallography. *BMC Biol.* **16**, 59 (2018).
- Rimmerman, D. et al. Direct observation of insulin association dynamics with time-resolved X-ray scattering. *J. Phys. Chem. Lett.* **8**, 4413–4418 (2017).
- Rimmerman, D. et al. Insulin hexamer dissociation dynamics revealed by photoinduced T-jumps and time-resolved X-ray solution scattering. *Photochem. Photobiol. Sci.* **17**, 874–882 (2018).
- Cho, H. S. et al. Dynamics of quaternary structure transitions in R-state carbonmonoxyhemoglobin are unveiled in time-resolved X-ray scattering patterns following a temperature jump. *J. Phys. Chem. B* **122**, 11488–11496 (2018).
- Frauenfelder, H., Fenimore, P. W. & Young, R. D. Protein dynamics and function: insights from the energy landscape and solvent slaving. *IUBMB Life* **59**, 506–512 (2007).
- Fenimore, P. W., Frauenfelder, H., McMahon, B. H. & Parak, F. G. Slaving: solvent fluctuations dominate protein dynamics and functions. *Proc. Natl Acad. Sci. USA* **99**, 16047–16051 (2002).
- Wang, J. & El-Sayed, M. A. Temperature jump-induced secondary structural change of the membrane protein bacteriorhodopsin in the premelting temperature region: a nanosecond time-resolved Fourier transform infrared study. *Biophys. J.* **76**, 2777–2783 (1999).
- Wang, T., Lau, W. L., DeGrado, W. F. & Gai, F. T-jump infrared study of the folding mechanism of coiled-coil GCN4-p1. *Biophys. J.* **89**, 4180–4187 (2005).
- Akasaka, K., Naito, A. & Nakatani, H. Temperature-jump NMR study of protein folding: ribonuclease A at low pH. *J. Biomol. NMR* **1**, 65–70 (1991).
- Gillespie, B. et al. NMR and temperature-jump measurements of de novo designed proteins demonstrate rapid folding in the absence of explicit selection for kinetics. *J. Mol. Biol.* **330**, 813–819 (2003).
- Yamasaki, K. et al. Real-time NMR monitoring of protein-folding kinetics by a recycle flow system for temperature jump. *Anal. Chem.* **85**, 9439–9443 (2013).
- Meadows, C. W., Balakrishnan, G., Kier, B. L., Spiro, T. G. & Klinman, J. P. Temperature-jump fluorescence provides evidence for fully reversible microsecond dynamics in a thermophilic alcohol dehydrogenase. *J. Am. Chem. Soc.* **137**, 10060–10063 (2015).
- Vaughn, M. B., Zhang, J., Spiro, T. G., Dyer, R. B. & Klinman, J. P. Activity-related microsecond dynamics revealed by temperature-jump Förster resonance energy transfer measurements on thermophilic alcohol dehydrogenase. *J. Am. Chem. Soc.* **140**, 900–903 (2018).
- Hori, T. et al. The initial step of the thermal unfolding of 3-isopropylmalate dehydrogenase detected by the temperature-jump Laue method. *Protein Eng.* **13**, 527–533 (2000).
- Eisenmesser, E. Z. et al. Intrinsic dynamics of an enzyme underlies catalysis. *Nature* **438**, 117–121 (2005).
- Caines, M. E. C. et al. Diverse HIV viruses are targeted by a conformationally dynamic antiviral. *Nat. Struct. Mol. Biol.* **19**, 411–416 (2012).
- Price, A. J. et al. Active site remodeling switches HIV specificity of antiretroviral TRIMCyp. *Nat. Struct. Mol. Biol.* **16**, 1036–1042 (2009).
- Virgen, C. A., Kratovac, Z., Bieniasz, P. D. & Hatzioannou, T. Independent genesis of chimeric TRIM5-cyclophilin proteins in two primate species. *Proc. Natl Acad. Sci. USA* **105**, 3563–3568 (2008).
- Wilson, S. J. et al. Independent evolution of an antiviral TRIMCyp in rhesus macaques. *Proc. Natl Acad. Sci. USA* **105**, 3557–3562 (2008).
- Keedy, D. A. et al. Mapping the conformational landscape of a dynamic enzyme by multitemperature and XFEL crystallography. *eLife* **4**, e07574 (2015).
- Fraser, J. S. et al. Hidden alternative structures of proline isomerase essential for catalysis. *Nature* **462**, 669–673 (2009).
- Otten, R. et al. Rescue of conformational dynamics in enzyme catalysis by directed evolution. *Nat. Commun.* **9**, 1314 (2018).
- Clark, G. N. I., Hura, G. L., Teixeira, J., Soper, A. K. & Head-Gordon, T. Small-angle scattering and the structure of ambient liquid water. *Proc. Natl Acad. Sci. USA* **107**, 14003–14007 (2010).
- Kjær, K. S. et al. Introducing a standard method for experimental determination of the solvent response in laser pump, X-ray probe time-resolved wide-angle X-ray scattering experiments on systems in solution. *Phys. Chem. Chem. Phys.* **15**, 15003–15016 (2013).
- Cammarata, M. et al. Impulsive solvent heating probed by picosecond X-ray diffraction. *J. Chem. Phys.* **124**, 124504 (2006).
- Gruebele, M., Sabelko, J., Ballew, R. & Ervin, J. Laser temperature jump induced protein refolding. *Acc. Chem. Res.* **31**, 699–707 (1998).
- Levantino, M. et al. Ultrafast myoglobin structural dynamics observed with an X-ray free-electron laser. *Nat. Commun.* **6**, 6772 (2015).
- DiCiccio, T. J. & Efron, B. Bootstrap confidence intervals. *Stat. Sci.* **11**, 189–212 (1996).
- Smith, C. A. et al. Population shuffling of protein conformations. *Angew. Chem. Int. Ed. Engl.* **54**, 207–210 (2015).
- Wapeesittipan, P., Mey, A., Walkinshaw, M. & Michel, J. Allosteric effects in catalytic impaired variants of the enzyme cyclophilin A may be explained by changes in nano-microsecond time scale motions. *Commun. Chem.* **2**, 41 (2019).
- Chi, C. N. et al. A structural ensemble for the enzyme cyclophilin reveals an orchestrated mode of action at atomic resolution. *Angew. Chem. Int. Ed. Engl.* **54**, 11657–11661 (2015).
- Kim, J. G. et al. Cooperative protein structural dynamics of homodimeric hemoglobin linked to water cluster at subunit interface revealed by time-resolved X-ray solution scattering. *Struct. Dynam.* **3**, 023610 (2016).
- Colombo, M. F., Rau, D. C. & Parsegian, V. A. Protein solvation in allosteric regulation: a water effect on hemoglobin. *Science* **256**, 655–659 (1992).
- Salvay, A. G., Grigera, J. R. & Colombo, M. F. The role of hydration on the mechanism of allosteric regulation: in situ measurements of the oxygen-linked kinetics of water binding to hemoglobin. *Biophys. J.* **84**, 564–570 (2003).

58. Royer, W. E. Jr, Pardanani, A., Gibson, Q. H., Peterson, E. S. & Friedman, J. M. Ordered water molecules as key allosteric mediators in a cooperative dimeric hemoglobin. *Proc. Natl Acad. Sci. USA* **93**, 14526–14531 (1996).
59. Fenwick, R. B., Oyen, D., Dyson, H. J. & Wright, P. E. Slow dynamics of tryptophan–water networks in proteins. *J. Am. Chem. Soc.* **140**, 675–682 (2018).
60. Grossman, M. et al. Correlated structural kinetics and retarded solvent dynamics at the metalloprotease active site. *Nat. Struct. Mol. Biol.* **18**, 1102–1108 (2011).
61. Decaneto, E. et al. Solvent water interactions within the active site of the membrane type I matrix metalloproteinase. *Phys. Chem. Chem. Phys.* **19**, 30316–30331 (2017).
62. Leidner, F., Kurt Yilmaz, N., Paulsen, J., Muller, Y. A. & Schiffer, C. A. Hydration structure and dynamics of inhibitor-bound HIV-1 protease. *J. Chem. Theory Comput.* **14**, 2784–2796 (2018).
63. Guha, S. et al. Slow solvation dynamics at the active site of an enzyme: implications for catalysis. *Biochemistry* **44**, 8940–8947 (2005).
64. Dahanayake, J. N. & Mitchell-Koch, K. R. Entropy connects water structure and dynamics in protein hydration layer. *Phys. Chem. Chem. Phys.* **20**, 14765–14777 (2018).
65. Wand, A. J. & Sharp, K. A. Measuring entropy in molecular recognition by proteins. *Annu. Rev. Biophys.* **47**, 41–61 (2018).
66. Caro, J. A. et al. Entropy in molecular recognition by proteins. *Proc. Natl Acad. Sci. USA* **114**, 6563–6568 (2017).
67. Gavrillov, Y., Leuchter, J. D. & Levy, Y. On the coupling between the dynamics of protein and water. *Phys. Chem. Chem. Phys.* **19**, 8243–8257 (2017).
68. Conti Nibali, V., D'Angelo, G., Paciaroni, A., Tobias, D. J. & Tarek, M. On the coupling between the collective dynamics of proteins and their hydration water. *J. Phys. Chem. Lett.* **5**, 1181–1186 (2014).
69. Hub, J. S. Interpreting solution X-ray scattering data using molecular simulations. *Curr. Opin. Struct. Biol.* **49**, 18–26 (2018).
70. Svergun, D. I. et al. Protein hydration in solution: experimental observation by X-ray and neutron scattering. *Proc. Natl Acad. Sci. USA* **95**, 2267–2272 (1998).
71. Virtanen, J. J., Makowski, L., Sosnick, T. R. & Freed, K. F. Modeling the hydration layer around proteins: applications to small- and wide-angle X-ray scattering. *Biophys. J.* **101**, 2061–2069 (2011).
72. Henriques, J., Arleth, L., Lindorff-Larsen, K. & Skepö, M. On the calculation of SAXS profiles of folded and intrinsically disordered proteins from computer simulations. *J. Mol. Biol.* **430**, 2521–2539 (2018).
73. Dellus-Gur, E. et al. Negative epistasis and evolvability in TEM-1  $\beta$ -lactamase—the thin line between an enzyme's conformational freedom and disorder. *J. Mol. Biol.* **427**, 2396–2409 (2015).
74. Biel, J. T., Thompson, M. C., Cunningham, C. N., Corn, J. E. & Fraser, J. S. Flexibility and design: conformational heterogeneity along the evolutionary trajectory of a redesigned ubiquitin. *Structure* **25**, 739–749.e3 (2017).
75. Fischer, M., Coleman, R. G., Fraser, J. S. & Shoichet, B. K. Incorporation of protein flexibility and conformational energy penalties in docking screens to improve ligand discovery. *Nat. Chem.* **6**, 575–583 (2014).
76. Fischer, M., Shoichet, B. K. & Fraser, J. S. One crystal, two temperatures: cryocooling penalties alter ligand binding to transient protein sites. *ChemBioChem* **16**, 1560–1564 (2015).
77. Keedy, D. A. et al. An expanded allosteric network in PTP1B by multitemperature crystallography, fragment screening, and covalent tethering. *eLife* **7**, e36307 (2018).
78. Fraser, J. S. et al. Accessing protein conformational ensembles using room-temperature X-ray crystallography. *Proc. Natl Acad. Sci. USA* **108**, 16247–16252 (2011).
79. Van den Bedem, H., Bhabha, G., Yang, K., Wright, P. E. & Fraser, J. S. Automated identification of functional dynamic contact networks from X-ray crystallography. *Nat. Methods* **10**, 896–902 (2013).

## Acknowledgements

We thank R. Ranganathan, J. Holton, G. Hura and D. Elnatan for helpful discussions, and the staff at the BioCARS beamline at the Advanced Photon Source (I. Kosheleva, R. Henning, A. DiChiara and V. Srajer) for assistance. This work was supported by the NSF (STC-1231306), the NIH (GM123159 and GM124149), a Packard Fellowship from the David and Lucile Packard Foundation, the UC Office of the President Laboratory Fees Research Program LFR-17-476732 (to J.S.F.), the Intramural Research Program of the National Institute of Diabetes and Digestive and Kidney Diseases (to P.A.) and a Ruth L. Kirschstein National Research Service Award (F32 HL129989 to M.C.T.). Use of the Advanced Photon Source was supported by the US Department of Energy, Basic Energy Sciences, Office of Science, under contract number DE-AC02-06CH11357. Use of the BioCARS Sector 14 was also supported by the NIH National Institute of General Medical Sciences (grant R24GM111072). The time-resolved setup at Sector 14 was funded in part through a collaboration with P.A. (NIH/NIDDK).

## Author contributions

M.C.T., P.A. and J.S.F. conceived and designed the experiments. M.C.T., B.A.B., A.M.W., H.S.C., F.S., D.M.C.S. and P.A. performed the experiments. M.C.T., B.A.B. and A.M.W. analysed the data. M.C.T., B.A.B., A.M.W., H.S.C., F.S. and P.A. contributed materials/analysis tools. M.C.T. and J.S.F. wrote the paper. All authors discussed the results and commented on the manuscript.

## Competing interests

The authors declare no competing interests.

## Additional information

**Supplementary information** is available for this paper at <https://doi.org/10.1038/s41557-019-0329-3>.

**Reprints and permissions information** is available at [www.nature.com/reprints](http://www.nature.com/reprints).

**Correspondence and requests for materials** should be addressed to P.A. or J.S.F.

**Publisher's note** Springer Nature remains neutral with regard to jurisdictional claims in published maps and institutional affiliations.

© The Author(s), under exclusive licence to Springer Nature Limited 2019

In the format provided by the authors and unedited.

# Temperature-jump solution X-ray scattering reveals distinct motions in a dynamic enzyme

Michael C. Thompson<sup>1</sup>, Benjamin A. Barad<sup>1,2</sup>, Alexander M. Wolff<sup>1,2</sup>, Hyun Sun Cho<sup>3</sup>,  
Friedrich Schotte<sup>3</sup>, Daniel M. C. Schwarz<sup>1,4</sup> , Philip Anfinrud<sup>3\*</sup> and James S. Fraser<sup>1\*</sup> 

---

<sup>1</sup>Department of Bioengineering and Therapeutic Sciences, University of California, San Francisco, San Francisco, CA, USA. <sup>2</sup>Biophysics Graduate Program, University of California, San Francisco, San Francisco, CA, USA. <sup>3</sup>Laboratory of Chemical Physics, National Institute of Diabetes and Digestive and Kidney Diseases, National Institutes of Health, Bethesda, MD, USA. <sup>4</sup>Chemistry and Chemical Biology Graduate Program, University of California, San Francisco, San Francisco, CA, USA. \*e-mail: [anfinrud@nih.gov](mailto:anfinrud@nih.gov); [jfraser@fraserlab.com](mailto:jfraser@fraserlab.com)

## SUPPLEMENTARY INFORMATION

### Temperature-Jump Solution X-ray Scattering Reveals Distinct Motions in a Dynamic Enzyme

Michael C. Thompson<sup>1</sup>, Benjamin A. Barad<sup>1,2</sup>, Alexander M. Wolff<sup>1,2</sup>, Hyun Sun Cho<sup>3</sup>, Friedrich Schotte<sup>3</sup>, Daniel M.C. Schwarz<sup>1,4</sup>, Philip A. Anfinrud<sup>3,#</sup>, James S. Fraser<sup>1,\*</sup>

<sup>1</sup>Department of Bioengineering and Therapeutic Sciences, University of California, San Francisco, San Francisco, CA 94158, USA

<sup>2</sup>Biophysics Graduate Program, University of California, San Francisco, San Francisco, CA 94158, USA

<sup>3</sup>Laboratory of Chemical Physics, National Institute of Diabetes and Digestive and Kidney Diseases, National Institutes of Health, Bethesda, MD 220892-0520, USA

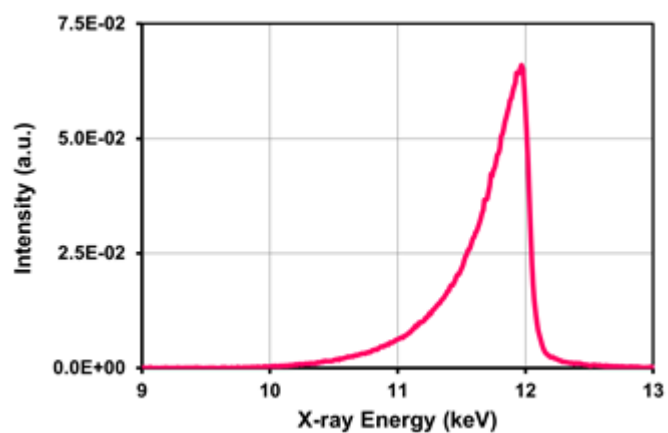
<sup>4</sup>Chemistry and Chemical Biology Graduate Program, University of California, San Francisco, San Francisco, CA 94158, USA

# - [anfinrud@nih.gov](mailto:anfinrud@nih.gov)

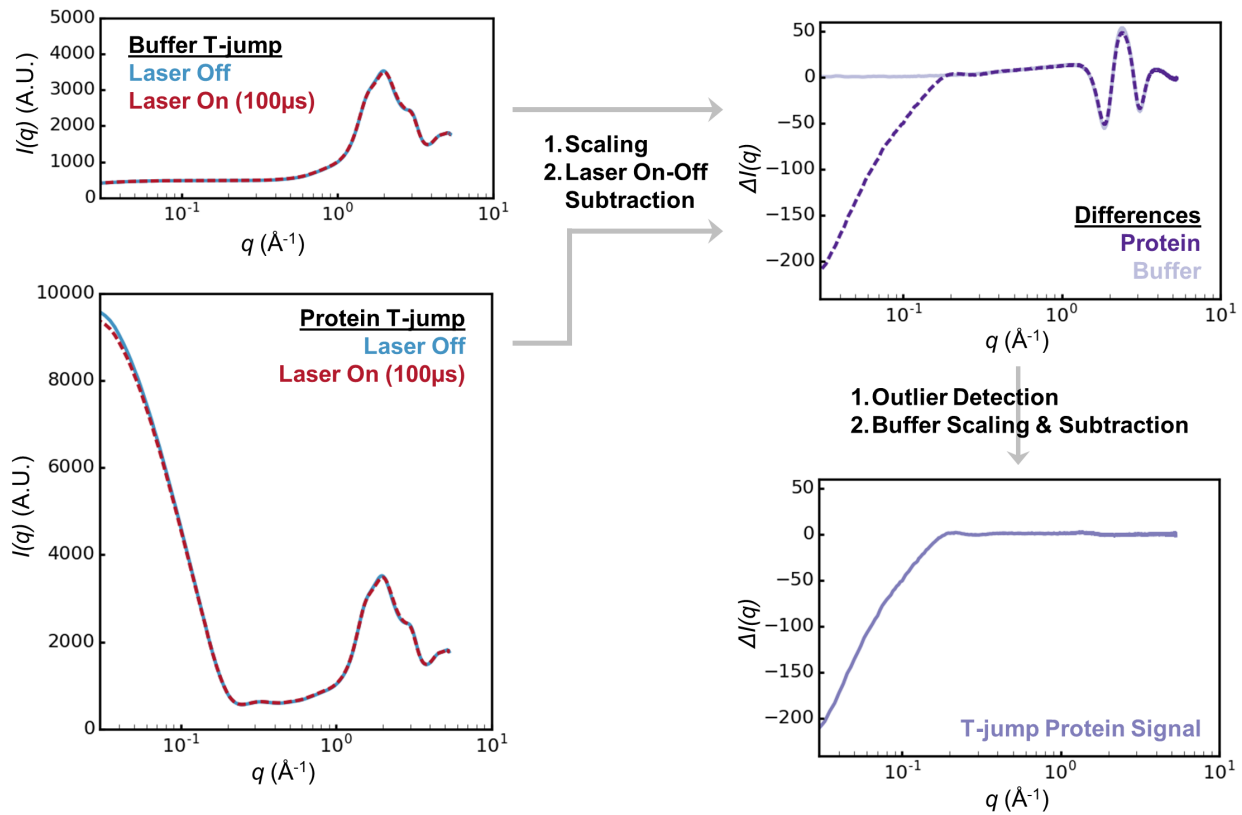
\* - [jfraser@fraserlab.com](mailto:jfraser@fraserlab.com)

#### Table of Contents

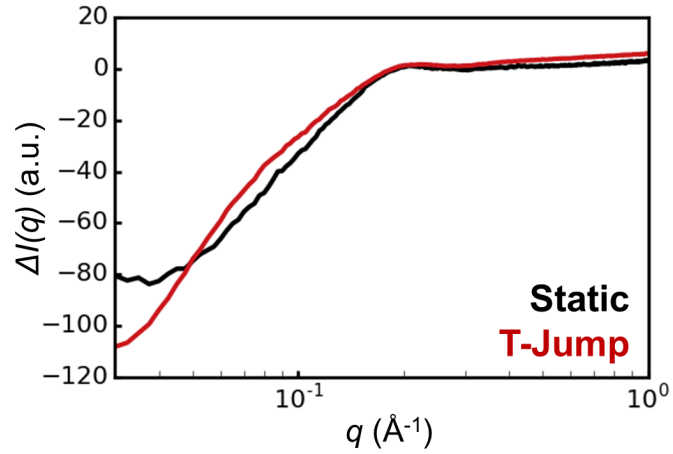
Supplementary Figures 1-8	pg 2-9
Supplementary Table 1	pg 10
Supplementary Data	pg 11-12
Supplementary Methods	pg 13-17
Supplementary References	pg 18



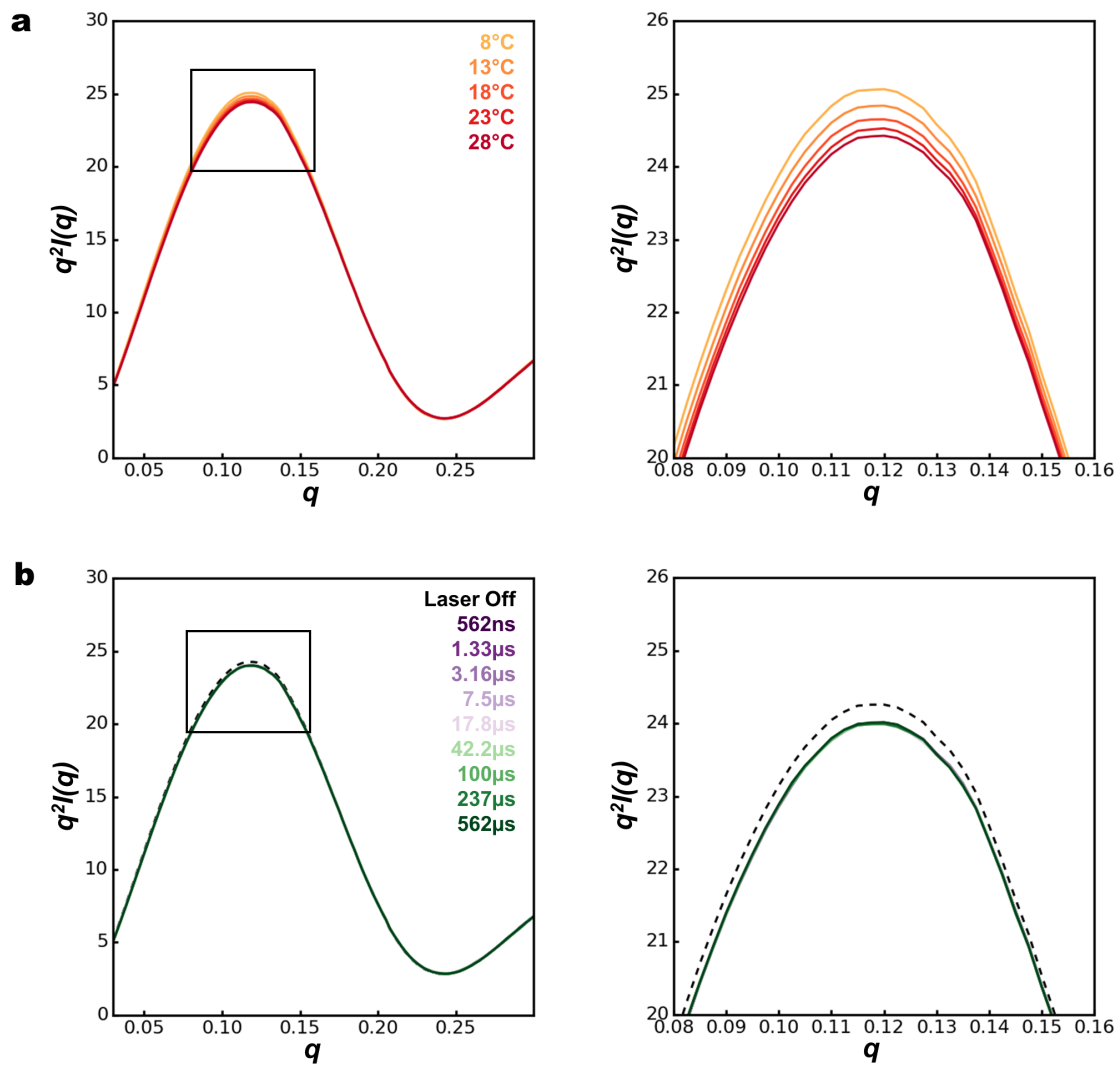
**Supplementary Figure 1. Pink beam energy spectrum.** Typical X-ray energy spectrum of the pink beam (3% energy bandwidth) used for the reported SAXS/WAXS measurements.



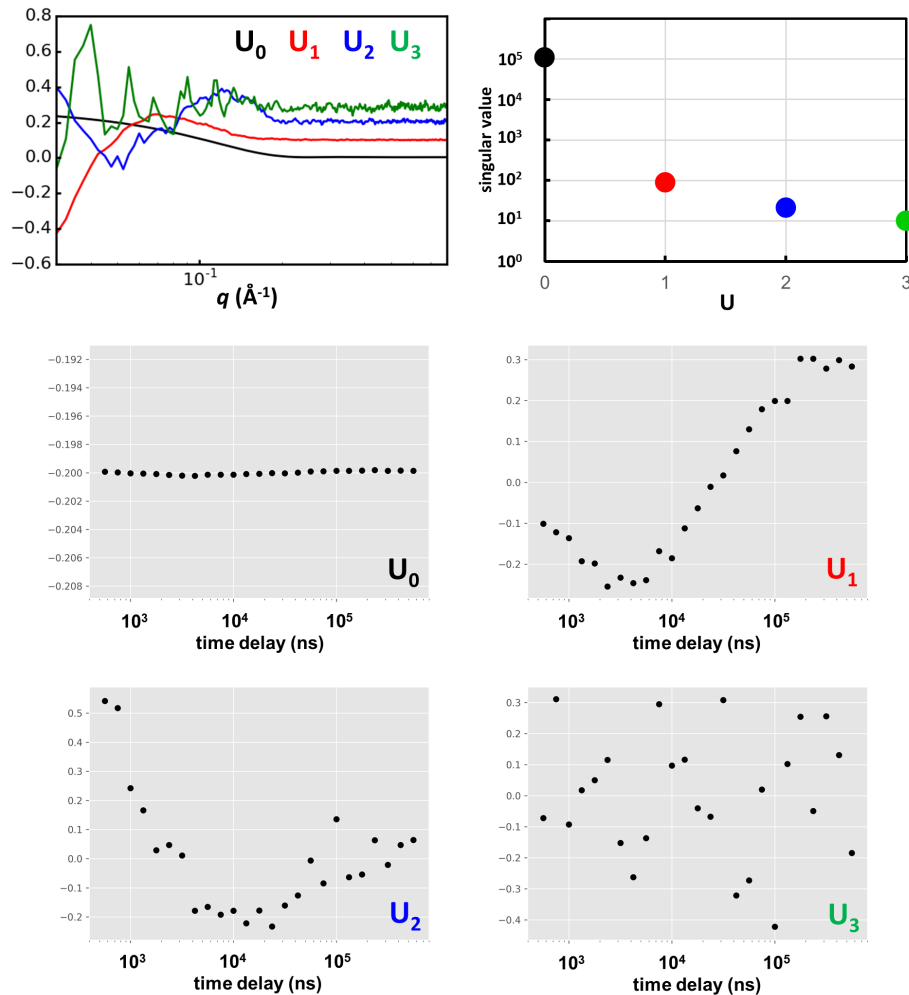
**Supplementary Figure 2. Reduction of T-jump SAXS/WAXS data.** T-jump data processing involves a combination of scaling and subtraction operations that produce time-resolved difference scattering curves. For each “laser on-off” pair, the recorded scattering curves are scaled to one another and the “laser off” curve is then subtracted from the “laser on” curve. This procedure is done independently for samples containing buffer only, and for protein samples. Next, the resulting difference curve for the buffer only sample is scaled to the difference curve obtained for the protein sample, and an additional buffer subtraction is performed to remove the thermal signal from the solvent. The result of this procedure is a difference scattering curve containing signal from the protein molecules only.



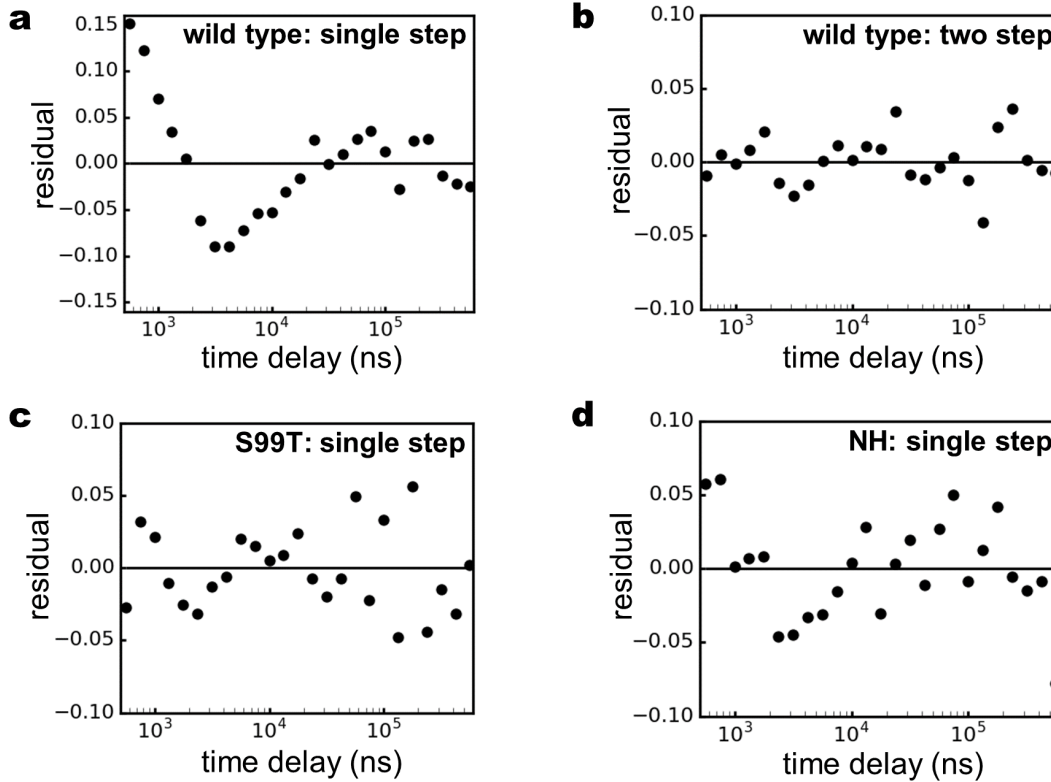
**Supplementary Figure 3. Comparison of static and time-resolved differences.** Static scattering differences between CypA solutions at 13°C and 23°C (black curve), and time resolved differences (100 $\mu$ s-laser off) for a T-jump spanning a temperature range of approximately 15°C and 26°C (red curve) are shown, demonstrating that the time-resolved signal equilibrates to approximately what would be expected based on static measurements.



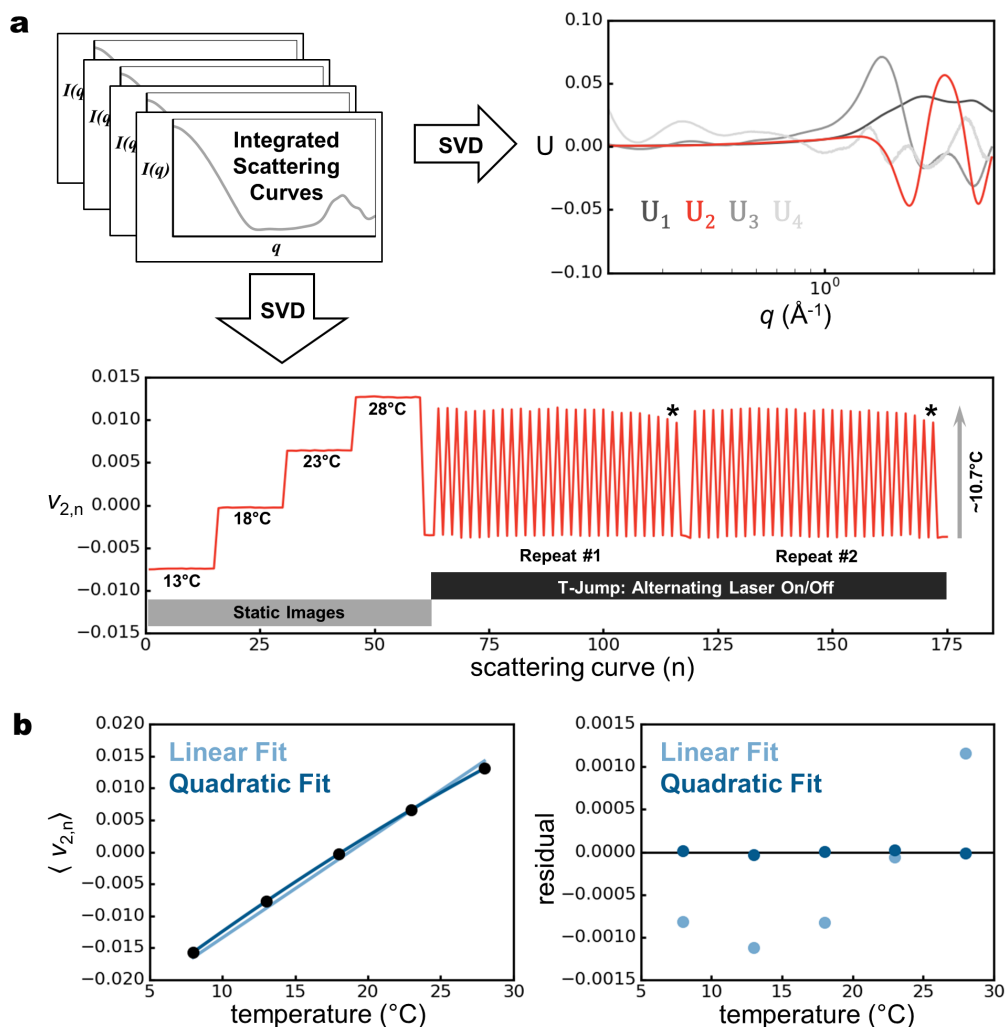
**Supplementary Figure 4. Kratky plots for CypA reveal a small thermal disorder effect without protein unfolding.** **a)** Kratky plots calculated as a function of static temperature, from 8°C to 28°C. The right panel shows an expanded view of the boxed region. **b)** Kratky plots calculated as a function of time delay for time-resolved T-jump data (colored lines, T-jump from approximately 15°C to 26°C). Again, the right panel shows an expanded view of the boxed region. All time delays show a similar difference relative to the “laser off” state (black dashed line), indicating that the underlying structural change is faster than the measurement dead time of our experiment.



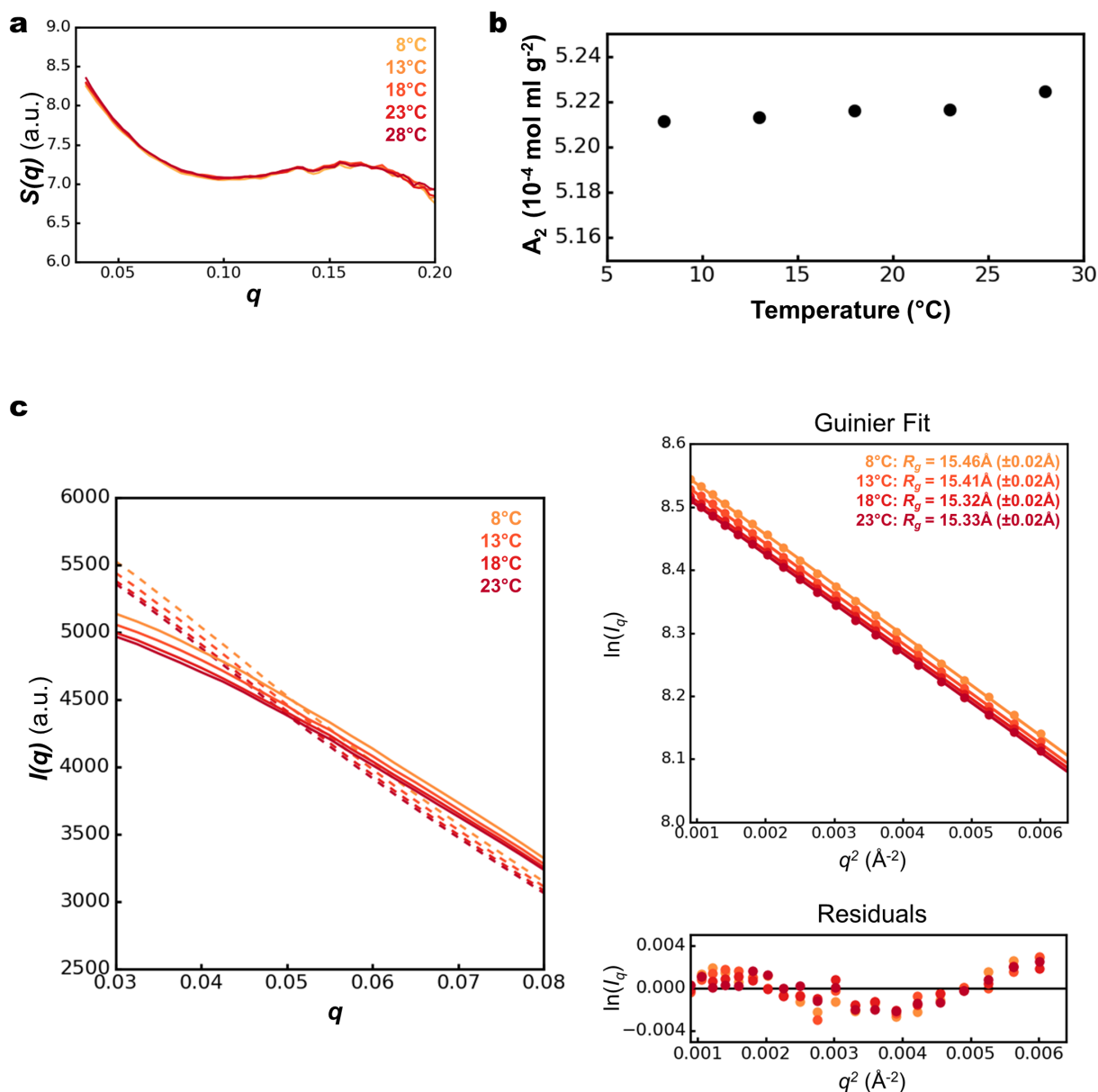
**Supplementary Figure 5. Kinetic analysis of X-ray scattering by singular value decomposition (SVD).** We used SAXS curves representing the time-resolved scattering at each time delay spanning 562ns and 562 $\mu$ s to construct a matrix, which was analyzed by SVD. The top left panel shows the top four left singular vectors ( $\mathbf{U}_n$ ), and the top right panel shows their corresponding singular values. The lower panels are constructed from the right singular vectors, and show the time-dependent contribution of each left singular vector to the total signal. We note that the primary time-resolved signal is contained in just one singular vector ( $\mathbf{U}_2$ ), whose time-dependent behavior reflects that of the integration analysis described in the main text.



**Supplementary Figure 6. Residuals for kinetic fits of T-jump SAXS/WAXS data for CypA variants.** Residuals are shown for the following variants and fitting procedures: **a**) Wild type, single-step relaxation. **b**) Wild type, two-step relaxation. **c**) S99T mutant, single-step relaxation. **d**) NH double mutant, single-step relaxation. When the wild type data are modeled using a single kinetic step (**a**), the residuals show structure indicative of a second exponential process. In contrast, other fits show residuals with random fluctuations about zero (**b**, **c**, **d**), indicating an appropriate number of steps were included in the kinetic models.



**Supplementary Figure 7. X-ray scattering from bulk water acts as a sensitive thermometer for T-jump experiments. a)** Using singular value decomposition (SVD), we can identify a signal whose contribution to each scattering curve is strongly dependent on the temperature. The left singular vectors with the four highest singular values are shown, with the vector corresponding to the temperature-dependent signal ( $U_2$ ) colored red. The contribution of this vector ( $v_{2,n}$ ) to each of 175 scattering curves is also shown. This set of 175 scattering curves includes static measurements (no pump laser) at four different temperatures, followed by two repeats of time-resolved T-jump measurements. The T-jump data were collected as “laser on-off” pairs, and within a single repeat each successive on-off pair was collected with an increasing pump-probe time delay. Cooling is evident at longer pump-probe time delays (denoted by \*). **b)** To calculate the magnitude of the laser-induced T-jump, we used the static data to determine the average value of  $v_{2,n}$  as a function of temperature, and fit the data using both linear and quadratic models. Based on the residuals for the two fits, we chose to use the resulting quadratic equation to determine the magnitude of the laser-induced T-jump using the values of  $v_{2,n}$  calculated for the time-resolved scattering curves by SVD.



**Supplementary Figure 8. Intermolecular interactions are not temperature dependent for CypA solutions.** A) Both structure factors ( $S(q)$  in panel a) and second virial coefficients ( $A_2$  in panel b) calculated for 50mg/mL CypA solutions (wild type) are unchanged over temperatures ranging from 8-28°C. Low angle scattering is affected by interparticle interactions (dashed lines in panel c, left), however the effects can be removed by “infinite dilution extrapolation” (solid lines in panel c, left). Guinier analysis (panel c, right) using the curves that are corrected for interparticle interactions shows that these effects can be successfully removed, and that the radius-of-gyration can be accurately determined at different temperatures.

CypA Variant	Temperature (°C)	Temperature (K)	$k_1$ ( $10^4$ s <sup>-1</sup> )	$k_2$ ( $10^4$ s <sup>-1</sup> )
WT	6.2 ± 0.2	279.2 ± 0.2	N/A	1.1 ± 0.3
WT	11.4 ± 0.2	284.4 ± 0.2	43 ± 7	1.2 ± 0.2
WT	15.9 ± 0.2	288.9 ± 0.2	49 ± 10	2.5 ± 0.3
WT	17.0 ± 0.1	290.0 ± 0.1	58 ± 11	1.6 ± 0.2
WT	21.5 ± 0.1	294.5 ± 0.1	57 ± 7	2.2 ± 0.2
WT	23.8 ± 0.2	296.8 ± 0.2	117 ± 33	2.2 ± 0.2
WT	25.5 ± 0.2	298.5 ± 0.2	53 ± 33	2.7 ± 0.9
WT	26.7 ± 0.1	299.7 ± 0.1	98 ± 12	2.5 ± 0.2
WT	29.9 ± 0.1	302.9 ± 0.1	116 ± 24	2.4 ± 0.2
S99T	25.5 ± 0.2	298.5 ± 0.2	34 ± 4	N/A
D66N/R69H	27.1 ± 0.1	300.1 ± 0.1	N/A	4.1 ± 0.6

**Supplementary Table 1.** Calculated rates for the fast ( $k_1$ ) and slow ( $k_2$ ) relaxation processes measured from all T-jump experiments reported here. Note that kinetic analyses for the S99T and NH variants were performed at 25.5°C and 27.1°C respectively.

## SUPPLEMENTARY DATA

### *Calibrating the Magnitude of the Temperature-Jump by Singular Value Decomposition*

To characterize the temperature-dependent behavior of the solvent scattering, we performed static SAXS/WAXS measurements of our CypA samples as a function of temperature (equilibrium, no IR laser), in addition to our time-resolved measurements. We pooled these static, temperature-dependent SAXS/WAXS curves (azimuthally integrated  $I(q)$  v.  $q$ ) with the time-resolved SAXS/WAXS curves from our T-jump measurements, and performed singular value decomposition (SVD) on a matrix constructed from the set of pooled curves (**Figure 7a**). Specifically, each column of this matrix represents a scattering curve, with each row of the matrix corresponding to a  $q$ -bin and the entries in the matrix corresponding to measured scattering intensities. The SVD analysis, which was performed over the  $q=0.07-3.45\text{\AA}^{-1}$  region of the scattering curves, identified a signal (a left singular vector) whose prominent features were found in the  $q$ -region corresponding to the scattering of bulk water ( $q > 1.0$ ) (**Figure 7a**). By extracting the entries in the corresponding row of the  $V$  matrix (containing the right singular vectors as columns), we could determine how this singular vector contributed to each scattering curve and demonstrate that its contribution was strongly temperature-dependent. Specifically, in the static (no T-jump) scattering curves the contribution of this singular vector increased with temperature, and for T-jump measurements the contribution of this vector to the observed scattering curves is perfectly correlated to the application of the pump laser pulse over sequential “laser on-off” pairs of X-ray measurements (**Figure 7a**), providing positive confirmation of a T-jump. Additionally, it is notable that the shape of the left singular vector used to monitor the temperature by SVD is nearly identical to that of the on-off difference signal at high- $q$ .

The identification of a temperature-dependent singular vector provided a simple way to measure the magnitude of the laser-induced T-jump<sup>1-5</sup>. For each of the five static temperatures we explored, we calculated the average value of  $v_{2,n}$ , the entry in the matrix  $V$  that describes the contribution of the temperature-dependent singular vector ( $U_2$ ) to the  $n$ th scattering curve, across 32 individual X-ray scattering curves. We then plotted the average  $v_{2,n}$  vs. temperature and fit the data using both linear and quadratic models (**Figure 7b**). We examined the residuals for the two fits, determined the quadratic fit produced the most appropriate “standard curve” for estimation of the sample temperature from the SVD analysis, and used the resulting second-degree polynomial to estimate the temperature for each scattering curve in our series of time-resolved measurements. We compared the temperatures calculated for neighboring “laser on” and “laser” off scattering curves, and found the average T-jump produced by our IR heating pulse to be approximately  $10.7^\circ\text{C}$ . We observed that  $v_{2,n}$  was consistent as a function of pump-probe time delay out to delay times of approximately  $562\mu\text{s}$ , and decreased for longer time delays, implying that significant cooling of the sample occurred in less than 1 millisecond. Consequently, we limited our subsequent analysis to time delays shorter than  $562\mu\text{s}$ .

Additional details about the temperature calibration are provided in the **Supplementary Methods** section.

### *Characterization of Interparticle Interactions and Structure Factor Corrections*

Because the main time-resolved signal change was confined to very low- $q$ , we wanted to ensure our time-resolved signal was due to a change in the protein’s form factor (infinite dilution), and not the structure factor of the protein solution. This process was challenging due to low signal-to-noise at high- $q$ , as well as our inability to measure very low-angle scattering using the available instrumentation. However, static measurements allowed us to identify the contribution of interparticle scattering, demonstrate that this contribution is invariant to temperature over the

range of our measurement conditions, and correct for its effect. To test whether changes in the radial distribution function originated from structural changes within the individual protein particles and their associated solvent and not from changes in the relative arrangement of the CypA molecules in solution, we performed static SAXS/WAXS measurements of CypA as a function of both temperature and CypA concentration. Using these data, we calculated the structure factor ( $S(q)$ ) for a 50mg/mL CypA solution at multiple different temperatures (see **Supplementary Methods**), and determined there was no significant difference in the  $q=0.03-0.2 \text{ \AA}^{-1}$  region of the scattering curves (**Figure 8**), consistent with other work on similarly-sized protein molecules in solution<sup>6</sup>. Next, we plotted the second virial coefficient for CypA as a function of temperature, and noticed that this quantity shows only a very small temperature dependence that cannot account for the observed time-resolved differences. In contrast to our results for CypA, Bonneté, et al. performed similar calculations of second virial coefficients for lysozyme solutions at similar temperatures and buffer conditions, and calculated temperature-dependent changes that were 50-fold larger (or more) than what we determined for CypA<sup>6</sup>. This analysis also allowed us to correct for the effects of interparticle interactions through a procedure which allows extrapolation of the observed concentration-dependent scattering to “infinite dilution” (see **Supplementary Methods**). In addition to the direct measurements of interparticle interactions provided by concentration-dependent scattering measurements, we also used Guinier analysis (linear fit of  $\ln[I(q)]$  vs.  $q^2$ , see **Supplementary Methods**) to assess whether the radial distribution function (structure factor) of CypA particles in solution changes significantly upon temperature perturbation. We analyzed scattering curves derived from both static temperature data and from time-resolved data, and observed that while Guinier fits of the T-jump measurements do have larger residuals than those for static data, the residuals do not change substantially as a function of either temperature (in static experiments) or time (in time-resolved experiments).

#### *Rapid Loss of X-ray Scattering Contrast due to Thermal Expansion*

We believe the largest contributor to the fast reduction in  $I(0)$  signal is thermal expansion, whose effect is twofold. First, thermal expansion of the system in general results in the expulsion of some scattering material (solvent containing CypA protein particles) from the X-ray beam path, which has a constant volume during the experiment. The volumetric thermal expansion coefficient of liquid water is approximately  $2.1 \cdot 10^{-4}/\text{K}$ <sup>7</sup>, and the sample is 95% water by mass, so the amount of material in the X-ray beam path decreases by approximately 0.2% for our T-jumps, which were approximately 11°C. Second, protein thermal expansion coefficients are estimated to be larger than those of liquid water, so heating of the sample results in a reduction of scattering density (loss of contrast) because the decrease in the average electron density of the protein particles is greater than that of the solvent. Using CypA crystal structures determined over a temperature range spanning 260-310K<sup>8</sup>, we determined the thermal expansion coefficient of CypA to be approximately  $4.1 \cdot 10^{-4}/\text{K}$ . The thermal expansion coefficient we calculated for CypA is similar to that of met-Myoglobin, which was reported to be  $3.5 \cdot 10^{-4}/\text{K}$  by<sup>9,10</sup>. Using our calculated thermal expansion coefficient for CypA and its average electron density calculated from a crystal structure, along with the analogous properties for bulk water<sup>7</sup>, we estimate that the  $I(0)$  change due to thermal expansion is approximately 2.6% for our T-jump experiments; however, this approximation likely overestimates the effect of thermal expansion on the scattering density of CypA particles, because we calculated the thermal expansion coefficient of the protein using a linear fit of volume versus temperature over a broad temperature range. In contrast, the thermal expansion coefficient likely has some temperature dependence and our analysis may overestimate thermal expansion in the relevant temperature regime.

## SUPPLEMENTARY METHODS

### *Sample Preparation*

CypA samples were prepared as described previously<sup>8,11</sup>. Briefly, the recombinant protein was expressed in *E. coli* BL21(DE3) cells and purified by liquid chromatography. Cells were lysed by sonication at pH=6.5, the lysate was clarified by high-speed centrifugation, and CypA was captured from the clarified lysate using a HiTrap-SP cation-exchange column (GE Healthcare). The protein was eluted using a sodium chloride gradient, and fractions containing CypA were pooled, and the pH was shifted to 7.5. The resulting solution was applied to a HiTrap-Q anion exchange column (GE Healthcare), and CypA was collected in the column flow-through. Finally, a polishing step was performed using a Superdex-75 gel filtration column (GE Healthcare). The protein was concentrated to 50mg/mL in buffer containing 20mM HEPES (4-(2-hydroxyethyl)-1-piperazine-ethanesulfonic acid) buffer at pH=7.5, 50mM sodium chloride, and 0.5mM TCEP (tris-hydroxyethylphosphine). CypA mutants (S99T and NH) were prepared following the same protocol used for the wild type protein. We note that while 50mg/mL is a relatively high protein concentration for in vitro experiments, this is much lower than the typical intracellular protein concentration (approximately 300mg/mL), and that CypA has been demonstrated to undergo its functional motions even in the crystalline environment<sup>8,11</sup>. For all X-ray measurements performed on buffer only without protein, the buffer was taken from the concentrator filtrate.

### *T-Jump SAXS/WAXS Data Collection and Processing*

Time-resolved SAXS/WAXS measurements of CypA were performed on the BioCARS beamline at the Advanced Photon Source, while the storage ring was operating in hybrid mode. Temperature-jump data were acquired using the pump-probe method, as described recently by Cho. et al.<sup>4</sup>. Fast temperature-jump was performed on a CypA solution (50mg/mL) in a silica capillary using an Opolette 355 II (HE) optical parametric oscillator (OPOTEK), which produced a 7ns laser pulse with a peak wavelength of 1443nm. The pump laser energy was approximately 1mJ per pulse, and the beam was focused to an elliptical spot with dimensions of 400 $\mu$ m by 60 $\mu$ m (FWHM, gaussian beam profile), yielding a photon fluence of ~50mJ/mm<sup>2</sup> at the sample, which heated a 50mg/mL CypA solution in a capillary. A suitably delayed X-ray pulse of 494ns duration (eight septuplets in APS hybrid mode) with a peak X-ray energy of 12keV and 3% energy bandwidth (pink beam, **Figure 1**), was used to probe the sample following the introduction of the T-jump, and the X-ray scattering was recorded using a Rayonix MX340-HS CCD detector. In our experiments, the temporal resolution is limited to approximately 500ns by the duration of the X-ray pulse, which is substantially longer than the duration of the IR pulse. To speed data acquisition, we utilized a sample holder and data collection scheme recently reported by Cho, et al.<sup>4</sup> which combined fast translation along the capillary axis with slow sample circulation via a peristaltic pump. The fast translation of the capillary allowed us to rapidly accumulate X-ray scattering from 41 pump-probe measurements on a single detector image by translating the capillary to a fresh position between each pump-probe pair. The slow circulation of the sample allowed us to replenish the protein solution and limit the extent of X-ray radiation damage by spreading the X-ray dose over a relatively large volume during long data collection runs. Data were collected as pairs of alternating "laser on" and "laser off" X-ray images. The pump-probe time delay was systematically increased with each successive on/off pair of images. We measured pump-probe time delays spanning three logarithmic decades from 562ns to 1ms, at a time density of eight points per decade. A total of 50 replicate X-ray images were collected for each pump-probe time delay. It is important to note that time-resolved X-ray measurements referred to herein as "laser off," were followed (10 $\mu$ s) by application of an IR pulse to the sample, as described by Cho, et al.<sup>4</sup>, which prevented the introduction of a temperature offset created by

incomplete cooling in between “laser on” and “laser off” measurements. A temperature controller integrated into the sample holder allowed us to initiate the T-jump from different starting temperatures, and also allowed us to collect static temperature data. Static temperature images were collected in a manner similar to the time-resolved images, but without application of the pump laser pulse. Data collection protocols were identical for protein and buffer samples.

After acquiring the data we applied polarization, geometry, and detector non-uniformity corrections to the 2D X-ray images. The scattering intensities (photons/pixel) were binned and averaged as a function of the scattering vector magnitude ( $q$ ), yielding isotropic scattering curves ( $I(q)$  vs.  $q$ ;  $q = 4\pi \cdot \sin(\theta)/\lambda$ , where  $2\theta$  is the scattering angle and  $\lambda$  is the X-ray wavelength)<sup>4</sup>. Next, for each data collection run, we carried out outlier detection by performing singular value decomposition (SVD) on a matrix constructed from our integrated scattering curves. In this SVD, the left singular vector with the largest singular value represents the global average of all the scattering curves used to construct the input matrix. We analyzed the right singular vectors from the SVD to determine which images were irregular. Specifically, we calculated the mean value of  $v_{1,n}$ , the entry in the matrix  $\mathbf{V}$  that describes the contribution of the right singular vector with the largest singular value ( $\mathbf{U}_1$ ) to the  $n^{\text{th}}$  scattering curve, across all the input X-ray scattering curves. Then, if the value of  $v_{1,n}$  for any specific scattering was more than 2.5 standard deviations above or below the mean, that image was discarded. Our outlier detection procedure is implemented in a Python script called “SVD\_Quarantine.py.” By inspecting the results of the SVD, we decided to remove the first 5 repeats from each data set, as well as some additional outliers that failed our statistical test. The same averaging and outlier detection method was used for both static and time-resolved measurements.

### *Scaling of X-ray Scattering Curves*

All scaling of X-ray scattering curves was performed using an algebraic (least-squares) procedure. To determine the scale factor,  $A$ , which can be applied to a scattering curve  $I(q)_a$  in order to scale it to a second scattering curve  $I(q)_b$ , we used the following equation:

$$A = \frac{\sum_q I(q)_a I(q)_b}{\sum_q I(q)_a^2} \quad \text{Eq. 2}$$

Although we used the equation above for scaling throughout our analysis, the  $q$ -range to which it was applied varied depending on the context, and details are provided below.

### *X-ray Thermometry*

Following the initial data processing steps described above, we used singular value decomposition (SVD) to determine the magnitude of the T-jump introduced by the IR laser pulse<sup>1-5</sup>. We pooled static, temperature-dependent SAXS/WAXS curves (azimuthally integrated  $I(q)$  v.  $q$ ) with the time-resolved SAXS/WAXS curves from time-resolved measurements, scaled them to a common reference over the  $q=0.025-4.28 \text{ \AA}^{-1}$  region, and performed SVD on a matrix built from these scaled curves. In this matrix, each column represents a single scattering curve, with the rows of the matrix corresponding to  $q$ -bins and the entries in the matrix consisting of azimuthally-averaged scattering intensities. The SVD analysis was performed using only the  $q=0.07-3.45 \text{ \AA}^{-1}$  region of the scattering curves. As described in the Results section, the SVD identified a left singular vector whose contribution to the overall scattering signal was highly temperature dependent. This was the left singular vector with the second largest singular value ( $\mathbf{U}_2$ ). For each of the five temperatures used for static data collection, we calculated the average value of  $v_{2,n}$ ,

which is the entry in the matrix  $V$  describing the contribution of the temperature-dependent singular vector ( $U_2$ ) to the  $n^{\text{th}}$  scattering curve. We then plotted the average  $v_{2,n}$  vs. temperature and ultimately fit this data using a quadratic model. Finally, we used the resulting second-degree polynomial and the values  $v_{2,n}$  for each time-resolved scattering curve to estimate the temperature for each T-jump measurement. By comparison of neighboring “laser on” and “laser off” scattering curves, we determined that the average T-jump was 10.7°C. Our thermometry procedure is implemented in a Python script called “thermometry\_timepoints.py.”

#### *Data reduction: On-Off Subtraction, Repeat Averaging, and Buffer Subtraction*

We implemented a data reduction procedure that operated on the integrated scattering curves generated using our data collection protocol and produced several outputs that were subsequently used for our kinetic and structural analyses. This procedure, implemented in a Python script called “reduce\_data.py,” took advantage of paired “laser on” and “laser off” measurements, redundant measurements of each pump-probe time-delay, and parallel T-jump experiments for samples containing protein and samples consisting of buffer only. The input for this script was essentially two data sets. The first, was a series of time-resolved scattering curves measured from a sample containing protein and consisting of paired “laser on/off” measurements with multiple replicate measurements of each pump-probe time delay (see above). The second was a similar data set, only collected from a sample containing buffer only and no protein. All of the input scattering curves were scaled to a common reference over the  $q=0.025-4.28\text{\AA}^{-1}$  range, and “laser off” curves were subtracted from their associated “laser on” curves to create a difference scattering curve ( $\Delta I(q)$ ) for each “laser on/off” pair. Next, all replicate difference curves (i.e. same sample and time delay) were grouped together, an iterative chi-squared test was performed (using a cutoff of  $\chi^2=1.5$ ), and the average difference curve was calculated for each pump-probe time delay in the series. For each time delay, the difference signal for the buffer only sample was scaled to the difference signal for the sample containing protein over the  $q=1.5-3.6\text{\AA}^{-1}$  range, and then the buffer signal was subtracted from the protein signal to isolate the difference signal due only to the protein. Additionally, this script took all of the “laser off” scattering curves, performed an iterative chi-squared test (cutoff of  $\chi^2=1.5$ ), and calculated their average. As was done for the difference curves, the average “laser off” scattering curve for buffer only was subtracted from the average “laser off” scattering curve for the protein sample after an additional scaling step ( $q=1.5-3.6\text{\AA}^{-1}$  range). The output of this data reduction procedure was a single scattering curve ( $I(q)$  vs.  $q$ ) for the “laser off” state, and a difference scattering curve ( $\Delta I(q)$  vs.  $q$ ) for each pump-probe time delay. All output data were corrected for the contribution of the buffer, and errors were propagated from the initial measurement standard deviations.

#### *Kinetic Analysis*

The averaged difference curves produced by our data reduction procedure were used for kinetic analysis of the time-resolved signal changes, which was implemented in a Python script called “difference\_dat\_kinetics.py.” For each time delay, this script integrated the area under the difference curve over the  $q=0.03-0.05\text{\AA}^{-1}$  range, then fit the resulting data (integrated area vs. time) to calculate relaxation rates using non-linear least-squares curve fitting. We used the following equations, for single-step kinetic fits:

$$A(1 - e^{-k_1 t}) + B \quad \text{Eq.3}$$

And for two-step kinetic fits:

$$A(1 - e^{-k_1 t}) + B(1 - e^{-k_2 t}) + C \quad \text{Eq. 4}$$

The output of this analysis was a relaxation rate, or two rates, with standard deviations calculated using a bootstrapping method<sup>12</sup>. The use of a bootstrap procedure was deemed appropriate, because standard deviations calculated for the integrated area under the difference scattering curves are likely to overestimate the true error, as they are the result of propagating measurement standard deviations through radial integration, scaling, on-off subtraction, averaging, buffer subtraction, and difference curve integration, with all experimental errors assumed to be random. In contrast, some experimental error is likely systematic, and would instead be removed, rather than propagated, by the subtractive operations employed during data processing. In cases where we performed T-jumps at multiple temperatures, we used the observed rates and their standard deviations to perform an Eyring analysis by fitting Eq. 1 (above) using a least-squares method to determine the enthalpy and entropy of activation, and their standard deviations (using the covariance matrix). We implemented the Eyring analysis in a Python script called “eyring\_fit.py.”

#### *Creation of High-Quality Time-Resolved Scattering Curves for Structural Analysis*

To produce high-quality scattering curves that could be used for real space interpretation of the time-resolved X-ray scattering, we took the following steps. We used all of the “laser off” scattering curves from our on-off paired time-resolved measurements to create a single average curve. Then, for each of the time-delays reported, we added the average on-off difference (see above) to this average “laser off” scattering curve:

$$I(q)_t = \langle I(q)_{off} \rangle + \langle \Delta I(q)_t \rangle \quad \text{Eq. 5}$$

Calculating the time-resolved scattering curves in this manner allows us to take advantage of the data collection structure, specifically the collection of “laser on and off” pairs, and many replicate measurements to remove some effects of systematic error that can accumulate during the course of long experiments and can mask small time-resolved differences in X-ray scattering. Next, we utilized static scattering measurements, as a function of both concentration and temperature, to characterize the effect of intermolecular interactions on the observed X-ray scattering and to calculate structure factors ( $S(q)$ ) for our 50mg/mL CypA solutions at temperatures spanning a range relevant to our T-jump experiments. We calculated structure factors (and second virial coefficients) following the methods described by Bonneté, et al. <sup>6</sup>. The scattering curves derived from summing the average “laser off” signal and the time-resolved differences were then divided by the calculated structure factors to correct for intermolecular interactions and extrapolate our measurements to infinite dilution. Because we discovered that the effect of intermolecular interactions was not temperature dependent, we did not need to model the time-dependence of structure factors for our protein solutions following the T-jump, and the structure factor calculated at 13°C was used for the infinite dilution extrapolation. The calculation of structure factors and the creation of the high-quality, corrected  $I(q)$  curves were implemented in a pair of Python scripts called “structure\_factor\_calc.py” and “structure\_factor\_correction\_TR.py,” respectively (a script called “structure\_factor\_correction\_static.py,” was used in the latter step for static data sets).

#### *Guinier Analysis and Calculation of $R_g$*

In order to calculate radii-of-gyration ( $R_g$ ) and to extrapolate the value of  $I(0)$  from scattering curves, we used the linear Guinier approximation:

$$\ln[I(q)] = \ln[I(0)] - \frac{R_g^2}{3} \cdot q^2 \quad \text{Eq. 6}$$

Guinier analysis was performed over the q-region spanning 0.03-0.08Å<sup>-1</sup>. We note that scattering curves were not placed on an absolute scale, however, this is not a requirement for Guinier analysis. The calculations were implemented in a Python script called “rg\_and\_i0.py.”

## SUPPLEMENTARY REFERENCES

1. Cammarata, M. *et al.* Impulsive solvent heating probed by picosecond x-ray diffraction. *J. Chem. Phys.* **124**, 124504 (2006).
2. Kjær, K. S. *et al.* Introducing a standard method for experimental determination of the solvent response in laser pump, X-ray probe time-resolved wide-angle X-ray scattering experiments on systems in solution. *Phys. Chem. Chem. Phys.* **15**, 15003–15016 (2013).
3. Arnlund, D. *et al.* Visualizing a protein quake with time-resolved X-ray scattering at a free-electron laser. *Nat. Methods* **11**, 923–926 (2014).
4. Cho, H. S. *et al.* Dynamics of Quaternary Structure Transitions in R-State Carbonmonoxyhemoglobin are Unveiled in Time-Resolved X-ray Scattering Patterns Following a Temperature Jump. *J. Phys. Chem. B* (2018). doi:10.1021/acs.jpcc.8b07414
5. Rimmerman, D. *et al.* Direct Observation of Insulin Association Dynamics with Time-Resolved X-ray Scattering. *J. Phys. Chem. Lett.* **8**, 4413–4418 (2017).
6. Bonneté, F., Finet, S. & Tardieu, A. Second virial coefficient: variations with lysozyme crystallization conditions. *J. Cryst. Growth* **196**, 403–414 (1999).
7. Irvine, T. F. & Duignan, M. R. Isobaric thermal expansion coefficients for water over large temperature and pressure ranges. *Int. Commun. Heat Mass Transfer* **12**, 465–478 (1985).
8. Keedy, D. A. *et al.* Mapping the conformational landscape of a dynamic enzyme by multitemperature and XFEL crystallography. *Elife* **4**, (2015).
9. Frauenfelder, H. *et al.* Thermal expansion of a protein. *Biochemistry* **26**, 254–261 (1987).
10. Hiebl, M. & Maksymiw, R. Anomalous temperature dependence of the thermal expansion of proteins. *Biopolymers* **31**, 161–167 (1991).
11. Fraser, J. S. *et al.* Hidden alternative structures of proline isomerase essential for catalysis. *Nature* **462**, 669–673 (2009).
12. DiCiccio, T. J. & Efron, B. Bootstrap confidence intervals. *Stat. Sci.* 189–212 (1996).